METTL3 regulates exocytosis independently of m^{6}A

Margalida Esteva-Socias[1,2†], Devi Prasad Bhattarai[1,2†], Cyrinne Achour[1,2†], Poonam Baidya[1,2], Gaia Fontanari[1,2], Kerstin Seier[2,3,4], Hudson Pace[2,3,4], Sandhya Malla[1,2], Shaochun Zhu[5], Eva Lundin[6], Cathrine Broberg Vågbø[7], Marta Bally[2,3,4], Vinay Swaminathan[8,9], André Mateus[5,10], Ruth Rodriguez-Barrueco[11], Andreas Pich[12], Francesca Aguilo[1,2*]

[1]Department of Molecular Biology, Umeå University, Umeå, Sweden
[2]Wallenberg Centre for Molecular Medicine, Umeå University, Umeå, Sweden
[3]Department of Clinical Microbiology, Umeå University, Umeå, Sweden
[4]Umeå Centre for Microbial Research, Umeå University, Umeå, Sweden
[5]Department of Chemistry, Umeå University, Umeå, Sweden
[6]Department of Medical Biosciences, Umeå University, Umeå, Sweden
[7]Proteomics and Modomics Experimental Core (PROMEC), Department of Clinical and Molecular Medicine, Norwegian University of Science and Technology (NTNU) and St. Olavs Hospital Central Staff, Trondheim, Norway.
[8]Division of Oncology, Department of Clinical Sciences, Lund University, Lund, Sweden
[9]Wallenberg Centre for Molecular Medicine, Lund University, Lund, Sweden
[10]The Laboratory for Molecular Infection Medicine Sweden (MIMS), Umeå, Sweden
[11]Departament de Patologia i Terapèutica Experimental, IDIBELL, Universitat de Barcelona, L'Hospitalet de Llobregat, Spain
[12]Research Core Unit Proteomics & Institute of Toxicology, Hannover Medical School, Hannover, Germany

[*]Correspondence to francesca.aguilo@umu.se

†These authors contributed equally

Running title: METTL3 regulates exocytosis

KEYWORDS: RNA modification, *N*^{6}-methyladenosine, METTL3, exocyst, EXOC7, breast cancer, vesicle trafficking

SUMMARY

RNA modification pathways are often mis-regulated in various cancers, with N6-methyladenosine (m^6A) having a pivotal role in cancer progression and metastasis. Methyltransferase-like 3 (METTL3), a core component of the m^6A methyltransferase complex, not only functions as an m6A writer but also promotes tumorigenesis through m6A-independent mechanisms. Here, we show that METTL3 is mislocalized to the cytoplasm in breast cancer tumors from patients, contributing to the oncogenic phenotype. Cytoplasmic METTL3 interacts with EXOC7, a key exocytosis regulator. Additionally, METTL3 regulates m^6A-dependent alternative splicing of EXOC7, promoting the expression of a more aggressive isoform. Silencing METTL3 impairs vesicle trafficking and the breast cancer secretome—effects that do not rely on its enzymatic activity but instead involve METTL3-mediated stabilization of EXOC7. Furthermore, METTL3 knockdown, but not inhibition of its catalytic function, impairs invadopodia formation, collagen matrix invasion, and focal adhesion morphology. Our findings uncover non-catalytic roles of METTL3 in regulating exocytosis and cancer secretome.

INTRODUCTION

RNA modifications have a crucial role in regulating gene expression. N^6-methyladenosine (m^6A), the most prevalent internal modification in messenger RNA (mRNA), is central to regulating the mRNA life cycle[1]. The core of the m^6A methyltransferase complex, mainly comprising METTL3 and METTL14, is responsible for depositing m^6A during transcription[2]. Dysregulation of m^6A homeostasis is associated with human diseases, including cancer[3,4]. Recent evidence suggests that in cancer cells, METTL3 can also be aberrantly localized to the cytoplasm, where it facilitates translation independently of its catalytic activity[5–9]. The precise role of METTL3 in tumorigenesis is complex and context-dependent, requiring further investigation into both its catalytic and non-catalytic functions.

In this study, we reveal that METTL3 is mislocalized to the cytoplasm in breast tumors, where it interacts with EXOC7 and other subunits of the exocyst, a protein complex that is critical for tethering secretory vesicles to the plasma membrane during exocytosis[10,11]. We further show that *EXOC7* undergoes m^6A-dependent alternative splicing, favoring the expression of a previously uncharacterized oncogenic isoform. Silencing of METTL3 in breast cancer cells resulted in decreased vesicle trafficking and an impaired breast cancer secretome, which is critical for tumor growth and metastasis. Notably, these effects persist despite enzymatic inhibition, as they result from METTL3-mediated stabilization of EXOC7, revealing a previously unrecognized non-catalytic function of METTL3. Additionally, we show that METTL3 silencing, independent of its methyltransferase activity, impairs the formation of invadopodia and reduces focal adhesion (FA) size—structures that are necessary for extracellular matrix (ECM) remodeling, cell migration and invasion, further supporting the broader impact of METTL3 beyond m^6A modulation.

Overall, these findings underscore the dual function of METTL3 in breast cancer, demonstrating that while its canonical role in m^6A deposition remains critical, its non-catalytic function in regulating exocytosis is also important. By directly influencing vesicle trafficking, METTL3 not only fuels tumor growth and metastasis but also redefines our understanding of its impact beyond RNA modification. Given the fundamental role of vesicle trafficking in multiple cancer types, METTL3-mediated exocytosis likely represents a widespread oncogenic mechanism, suggesting its broader significance beyond breast cancer.

RESULTS

METTL3 promotes breast cancer growth and metastasis

We have previously shown that silencing METTL3 leads to decreased proliferation, reduced colony formation, and increased apoptosis in breast cancer cell lines, indicating that METTL3 has a role in breast tumorigenesis[12]. To further explore the oncogenic role of METTL3 in vivo, we injected METTL3-depleted and scramble control MDA-MB-231 cells into the mammary fat pads of athymic nude mice (**Figure S1a**). No significant differences in weight were observed between the two groups of mice over three weeks (**Figure S1b**). However, the xenograft tumors derived from METTL3-knockdown cells exhibited a significant reduction in weight and volume compared to controls (**Figure 1a,b** and **Figure S1c**). Consistent with these findings, immunohistochemistry (IHC) staining with Ki67 revealed a marked reduction in cell proliferation in the METTL3-knockdown tumors (**Figure 1c,d**).

We next performed wound healing assays to investigate the metastatic potential of METTL3 in vitro. Silencing METTL3 led to a significant decrease in cell migration (**Figure 1e,f**). To assess its role in metastatic colonization in vivo, we performed experimental metastasis assays by injecting METTL3-knockdown and control cells into the tail vein of athymic nude mice. METTL3 depletion delayed lung metastasis formation compared to controls (**Figure 1g,h** and **Figure S1d,e**). IHC staining with Ki67 in lung metastases further confirmed reduced proliferation in the METTL3-knockdown group (**Figure 1i,j**). In conclusion, these findings suggest that METTL3 promotes both breast cancer growth and metastasis in vitro and in vivo.

METTL3 accumulates in breast cancer cell cytoplasm

We next interrogated the protein levels of METTL3 by performing IHC staining on a breast cancer tissue microarray (TMA). The TMA consisted of 100 cases of invasive ductal carcinoma and 10 adjacent healthy epithelial tissues. Our analysis revealed that METTL3 was present in both the nucleus and the cytoplasm in breast cancer samples whereas it predominantly localized in the nucleus of healthy epithelial tissues (**Figure 2a**). We further assessed staining intensity in these cellular compartments (**Figure S2a,b**). Although the nuclear expression of METTL3 did not differ significantly between breast cancer and normal tissues, we observed an accumulation of METTL3

in the cytoplasm across all breast cancer subtypes that we analysed (**Figure 2b,c**). Furthermore, we investigated the expression of METTL3 in a TMA containing normal healthy samples from various tissues. In these tissues, METTL3 predominantly localized to the nuclei, except in the bladder, lung and pancreas, where it also showed cytoplasmic accumulation (**Figure 2d**).

To further investigate the localization of METTL3, we examined nuclear and cytoplasmic subcellular fractions from breast cancer cells (MCF7 and MDA-MB-231) and normal breast epithelial cells (MCF10A and hTERT-HME1) by western blot and immunofluorescence analysis. Unlike the patient specimens, METTL3 was found in both the nuclei and cytoplasm of both cancerous and non-cancerous cell lines (**Figure S2c,d**). Together, these findings indicate that METTL3 localizes to the nuclei of healthy tissues, and that cell culture models do not accurately reflect the normal distribution observed in vivo.

METTL3 interacts with the exocyst complex

To gain insights into the function of cytoplasmic METTL3, we isolated cytoplasmic fractions from MCF7 cells and performed immunoprecipitation of endogenous METTL3 followed by liquid chromatography-tandem mass spectrometry (LC-MS/MS) (**Figure S3a**). Our analysis identified METTL3 (bait) and several known components of the writer complex, including METTL14, WTAP, and VIRMA (**Figure 3a, Figure S3b, Suppl. Table 1**). Notably, we also detected components of the exocyst complex, a conserved octameric complex that mediates the tethering of secretory vesicles to the plasma membrane for exocytosis[10,13]. Gene Ontology (GO) analysis of the cytoplasmic METTL3 interactome further supported the enrichment of terms related to both the exocyst complex and the m^6A methyltransferase complex, with relevant biological processes including mRNA methylation, protein transport, and vesicle docking (**Figure S3c**).

Given its functional relevance in cell migration and invasion [12,14–16], we focused on the interaction of METTL3 with EXOC7, one of the most enriched METTL3-interacting proteins identified. To conduct our investigation, we utilized the MDA-MB-231 cell line as it is a well-established model for studying triple-negative breast cancer (TNBC), known for its aggressive and highly invasive nature. Our analysis revealed the presence of both METTL3 and METTL14 in the nuclei and cytoplasm. Similarly, EXOC7 localized to these compartments, although it was less abundant in the nuclei (**Figure S3d**).

To confirm the interaction between METTL3 and EXOC7, we performed immunoprecipitation experiments of endogenous METTL3 in cytoplasmic fractions of MDA-MB-231 cells (**Figure 3b**, left panel). Notably, in the reverse co-immunoprecipitation of endogenous EXOC7, we did not detect METTL14, suggesting that METTL3 may be part of distinct protein complexes, as previously suggested (**Figure 3b**, right panel)[17]. In line with this observation, we did not retrieve EXOC7 upon METTL14 immunoprecipitation (**Figure 3c**). Furthermore, our analysis extended to a broader range of normal and cancer cell lines, where we previously assessed the cytoplasmic localization of METTL3 and EXOC7 (**Figure S3e-g**). We observed interactions between METTL3 and EXOC7 in the ovarian cancer cell line OVCAR8, HEK293T and hTERT-HME1 cells. However, no interaction was detected in mouse embryonic stem cells and U2OS cells, suggesting that the METTL3-EXOC7 interaction is context-dependent and may have varying biological roles depending on the cell type. To further confirm the physical interaction between these proteins, we performed *in vitro* pull-down assays (**Figure S3h**). These experiments provided additional evidence supporting the direct interaction between METTL3 and EXOC7, and further revealed that the leader helix region of METTL3 is crucial for this interaction (**Figure 3e,f**). Overall, these findings identified EXOC7 as a novel interactor of METTL3.

m^{6}A regulates *EXOC7* alternative splicing and EXOC7 protein stability

EXOC7 isoform switching has been observed in specific cellular contexts[16,18,19]. Based on exon 7 inclusion, *EXOC7* isoforms are classified into long isoforms (containing exon 7; isoforms 1, 4 and 6) and short isoforms (lacking exon 7; isoforms 2 and 5) (**Figure S4a**). *EXOC7* isoforms exhibit distinct expression patterns across various cell lines, with isoform 4 undetected in our cellular models (**Figure S4b,c**). The transition between short isoforms plays a role in epithelial-mesenchymal transition (EMT) in breast cancer, with isoform 2 promoting EMT and metastasis, while isoform 5 reduces cell motility[18].

We previously demonstrated that METTL3 regulates *EXOC7* AS, though we did not determine whether this regulation relies on its enzymatic activity[12]. Consistent with our prior findings, METTL3 depletion led to a marked reduction in the expression of the long isoform 6, while the levels of other isoforms remained largely unaffected (**Figure 4a,b**). To further investigate whether this regulation depends on the m^{6}A methyltransferase activity of METTL3, we conducted

additional experiments using the specific METTL3 inhibitor, STM2457[20]. METTL3 inhibition in MDA-MB-231 cells was validated by measuring m^6A levels on polyA-enriched RNA using mass spectrometry (**Figure S4d**). Additionally, pharmacological inhibition of METTL3 resulted in reduced cell proliferation and impaired wound healing (**Figure S4e,f**). Similar to METTL3 silencing, treatment with METTL3 inhibitor also led to reduced expression of the long isoform 6, indicating that METTL3 controls *EXOC7* AS in an m^6A-dependent manner (**Figure 4c**). For clarity, we will hereafter refer to isoform 6 as the long isoform and isoform 2 as the short isoform.

We next assessed the function of EXOC7 isoforms in MDA-MB-231 cells. Overexpression of the long and short isoforms revealed distinct localization patterns, with the long isoform primarily at the membrane and the short isoform distributed in both the membrane and cytoplasm (**Figure S5a,b**). Both isoforms promoted tunneling nanotube (TNTs) elongation, enhancing long-distance, contact-mediated intercellular communication, with the long isoform exerting a more pronounced effect (**Figure 5c,d**). Similarly, their overexpression promoted invadopodia formation—F-actin-rich protrusions involved in extracellular matrix (ECM) degradation and cancer cell invasiveness (**Figure S5e,f**). Quantification of ECM degradation areas showed reduced invadopodia activity upon EXOC7 silencing, as previously described (**Figure S5g-i**)[21].

When assessing EXOC7 protein levels, we observed a substantial decrease in the long isoform in METTL3 knockdown cells and inhibitor-treated cells, consistent with splicing defects, while the shorter isoform was slightly reduced only in the knockdowns (**Figure 4d,e**). To explore whether this reduction was linked to protein stability, we treated METTL3 knockdown cells with cycloheximide (CHX) and monitored EXOC7 protein levels over time. METTL3 depletion significantly shortened the half-life of both isoforms (**Figure 4f-h**), an effect not seen with enzymatic inhibition (**Figure 4i-k**). As METTL3 stabilizes several binding partners, including METTL14, WTAP and p53[22–24], these findings suggest that METTL3 may influence EXOC7 stability through a mechanism independent of its catalytic activity.

Given the role of METTL3 in EXOC7 protein stability, we next investigated exocyst complex assembly by performing non-reducing gel electrophoresis in control and METTL3 knockdown cells. Immunoblotting for EXOC7 revealed a decrease in both its oligomeric form (migrating above 250 kDa) and its monomeric form (at ~70 kDa) in METTL3 knockdown cells (**Figure 4l**).

Notably, this reduction observed under non-reducing conditions mirrored the decrease seen in conventional reducing gel electrophoresis (**Figure 4m**), indicating that METTL3 knockdown disrupts EXOC7 levels and consequently impairs exocyst complex formation. However, treatment of MDA-MB-231 cells with STM2457 did not recapitulate the effects observed in METTL3 knockdown cells (**Figure 4n,o**). Altogether, these findings highlight METTL3 as a key regulator of *EXOC7* AS through its catalytic activity and of EXOC7 protein stability via its scaffolding function, thereby influencing exocyst complex assembly.

METTL3 controls vesicle trafficking and secretion

Given that EXOC7 regulates the exocytosis of post-Golgi secretory vesicles at the plasma membrane[25], we sought to determine whether METTL3 influences vesicle trafficking. To this end, we monitored the transport of the transmembrane cargo protein vesicular stomatitis virus G protein (VSV-G) from the endoplasmic reticulum (ER) to the plasma membrane using the temperature-sensitive GFP-VSV-G^{ts045} construct[26]. At 40 °C, VSV-G is misfolded and retained in the ER; at 20 °C, it accumulates in the Golgi apparatus, and upon shifting to 32 °C, it is transported to the plasma membrane. To assess vesicle fusion with the plasma membrane, we performed immunostaining on non-permeabilized cells with the 8G5 monoclonal antibody, which specifically recognizes the extracellular domain of VSV-G. Quantifying and normalizing the surface VSV-G levels relative to total cellular levels revealed a 20-25% reduction in GFP-VSV-G^{ts045} incorporation into the plasma membrane following METTL3 silencing, suggesting that METTL3 is involved in VSV-G exocytosis (**Figure 5a** and **Figure S6a**). Similar results were observed with EXOC7 knockdowns (**Figure S6b,c**). However, treatment with the METTL3 inhibitor did not affect VSV-G secretion (**Figure 5b** and **Figure S6d**).

Breast cancer cells secrete a diverse array of substances referred to as the secretome, which have been implicated in tumor development and invasion[27–29]. Considering the negative impact of METTL3 silencing on vesicle trafficking, we investigated the secretome of control and METTL3-depleted MDA-MD-231 cells by performing mass spectrometry analysis of the conditioned media. We also conducted secretome analysis of EXOC7 knockdowns and cells treated with the METTL3 inhibitor STM2457. Protein hits were filtered to select secreted proteins, containing a signal peptide and without a transmembrane domain according to Uniprot database[11]. Consistent with the

defect in vesicle trafficking, we observed a reduction in protein secretion in both METTL3 and EXOC7 knockdowns compared to the scramble control (**Figure S6e-g** and **Suppl. Table 2**). Notably, STM2457-treated cells showed only mild changes in the secretome, with both increases and decreases in secreted proteins (**Figure S6h**). This suggests that the methyltransferase activity of METTL3 has a limited role in regulating the MDA-MB-231 cell secretome. Moreover, while strong correlations were observed between the METTL3-dependent and EXOC7-dependent secreted proteins, this correlation was lost when comparing the secretomes of both METTL3 and EXOC7 knockdown cells to those of cells treated with the METTL3 inhibitor (**Figure 5c-e**).

The overlap between the upregulated secretome in METTL3 knockdowns and STM2457 treatment was negligible (**Figure 5f**). In contrast, 97.5% of proteins with reduced secretion in the non-m^6A-dependent secretome overlapped with those showing reduced secretion in EXOC7 knockdowns (**Figure 5g,h**). Gene ontology (GO) analysis revealed that these downsecreted proteins were enriched in biological processes crucial in cancer progression, including ECM organization, cell adhesion, and collagen fibril formation (**Figure 5i**). Several of these proteins, such as PLOD2, matrix metalloproteinase 1 (MMP1), IL-6, FSTL1, CTSC and EFEMP1, have previously been identified in the breast cancer secretome regulating the metastatic ability of these tumors[30–35]. To further investigate these findings, we assessed MMP1 protein levels in both cellular extracts and culture media. Consistent with the secretome analysis, METTL3 knockdown led to a significant reduction in MMP1 secretion (**Figure 5j**), while STM2457 treatment did not elicit the same effect (**Figure 5k**).

Altogether, these findings suggest that METTL3 and EXOC7 jointly regulate the secretion of proteins involved in cancer progression, with METTL3's function extending beyond its methyltransferase activity.

METTL3 enhances ECM degradation for tumor invasion

Cancer cell invasiveness relies heavily on their ability to degrade the surrounding ECM. In METTL3-knockdown cells, downsecreted proteins—independent of m^6A modification—were notably enriched in ECM organization categories. To explore this further, we performed a matrix degradation (invadopodia) assay by plating control and METTL3-knockdown MDA-MB-231 cells

onto fluorescent-gelatin-coated coverslips. Quantification of degradation areas showed that METTL3-knockdown cells had reduced invadopodia activity, reflecting impaired ECM degradation (**Figure 6a,b**). However, treatment with STM2457 did not have any effect on invadopodia activity (**Figure 6c,d**), suggesting that the m^6A methyltransferase activity of METTL3 is not crucial for mediating ECM degradation.

To assess METTL3 specificity in regulating invadopodia formation, we engineered a doxycycline-inducible METTL3 cell line that cannot be targeted by shRNA2 and fused to a nuclear export signal (NES) (**Figure S7a,b**). This enabled the depletion of endogenous METTL3 while maintaining cytoplasmic METTL3 expression (hereafter referred to as METTL3-cyto). Additionally, to dissect the catalytic from the non-catalytic functions, the catalytic center of METTL3 was mutated in the same cellular system (*aa395–398, DPPW → APPA*) (METTL3-cyto_mut) (**Figure S7a,b**). As previously observed, METTL3 knockdown reduced EXOC7 protein levels, with a more pronounced effect on the long isoform (**Figure S7c,d**). Reintroduction of both wild-type and mutant cytoplasmic METTL3 rescued the expression of the short EXOC7 isoform, while only wild-type METTL3 restored the long isoform (**Figure S7c,d**), confirming the involvement of m^6A in exon 7 inclusion of EXOC7. METTL3-cyto_mut interacted with EXOC7, indicating that the intact catalytic domain of METTL3 is not required for such interaction (**Figure S7e**). Notably, treatment with the STM2457 inhibitor did not disrupt the interaction between EXOC7 and METTL3 (**Figure S7f**). Following endogenous METTL3 silencing, re-expression of both METTL3-cyto and METTL3-cyto_mut effectively rescued the invadopodia phenotypes (**Figure 6e-h**), confirming that the interaction between METTL3 and EXOC7, rather than its m^6A methyltransferase activity, is necessary for this process. Interestingly, both METTL3-cyto and METTL3-cyto_mut also restored the vesicle trafficking defect observed in METTL3 knockdowns, demonstrating that the cytoplasmic function of METTL3 is crucial for mediating exocytosis (**Figure 6i,j** and **Figure S7g,h**).

To further investigate the role of METTL3-EXOC7 binding in regulating invadopodia formation, we examined the LH domain of METTL3, that we previously identified as critical for this association. We depleted endogenous METTL3 and introduced a METTL3 variant lacking the LH domain (METTL3-ΔLH), which was unable to interact with EXOC7 (**Figure S7i,j**). Notably, re-

expression of METTL3-ΔLH failed to restore invadopodia formation, highlighting the importance of METTL3-EXOC7 interaction in this process (**Figure 6k,l**).

Consistently, METTL3 silencing prevented the enhanced formation of invadopodia upon both short and long overexpression of EXOC7 (**Figure S8a-d**), and effect that was not observed following STM2457 treatment (**Figure S8e-h**). Similarly, the formation of elongated TNTs was abolished when using an siRNA against METTL3 but persisted with STM2457 treatment (**Figure S9a-d**). These findings confirm that, beyond regulating *EXOC7* AS via m^6A modification, METTL3 influences EXOC7 function through a catalytic-independent mechanism.

We then generated tumor-derived spheroids, 3D cultures that mimic the in vivo growth conditions of cancer and evaluated their ability to invade a collagen-rich ECM, simulating the tumor microenvironment. Notably, spheroid growth was completely abolished after 24 h of culture following METTL3 silencing (**Figure 7a,b**), whereas no significant changes in growth were observed with METTL3 inhibitor treatment (**Figure 7c,d**), even after extended culture periods. Furthermore, METTL3 knockdown cells lost their ability to invade the collagen matrix (**Figure 7e,f**), while treatment with the STM2457 inhibitor resulted in only a modest, non-significant reduction in matrix invasion (**Figure 7g,h**).

Cells sense and respond to ECM cues—such as composition, density, stiffness, viscoelasticity, and architecture—by generating forces at FA sites, which are transmitted downstream via mechanotransduction to regulate migration. To assess whether METTL3 depletion affects FA, scramble control, METTL3 knockdown, DMSO-treated, and STM2457-treated cells were seeded on collagen-coated coverslips and incubated for 24 h to allow FAs to form. Following incubation, cells were fixed and subjected to paxillin immunostaining, as paxillin is a key scaffold protein that localizes to FA, regulating their assembly, maturation, and signaling[36]. Immunofluorescence analysis revealed significant differences in cell morphology between scramble control and METTL3 knockdown cells, with the latter exhibiting a significantly reduced cell spread area (**Figure7 i,k**). In contrast, STM2457-treated cells displayed a modest increase in cell area compared to DMSO-treated controls (**Figure 7j,l**). However, when examining FA size, only shRNA2 showed a reduction relative to control cells (**Figure 7m**). To address inconsistencies observed with the first two METTL3 shRNAs, a third shRNA targeting the 3'UTR of

METTL3 was included, confirming a reduction in FA size. Notably, the pharmacological inhibition of METTL3 had no significant effect (**Figure 7n**). Altogether these findings underscore the critical role of METTL3 in regulating the secretion of proteins associated with ECM invasion, ECM organization and cell adhesion, independent of its m^6A methyltransferase activity.

Discussion

In this study, we have uncovered a function of METTL3 in promoting exocytosis, extending its role beyond its well-established activity as an m^6A methyltransferase. Abnormal expression of METTL3 and dysregulated m^6A modification have been linked to various human diseases, including breast cancer[37]. Here we provide evidence that METTL3 also contributes to breast tumorigenesis through m^6A-independent mechanisms by regulating exocytosis via the exocyst complex.

Silencing METTL3 in breast cancer models resulted in impaired tumor growth and reduced lung metastasis, highlighting its critical role in breast cancer progression and metastasis. Additionally, we observed cytoplasmic accumulation of METTL3 in breast cancer cells from patients, whereas in normal breast epithelial cells, METTL3 was predominantly nuclear, suggesting a shift in its subcellular localization during cellular transformation. Consistent with this, METTL3 was primarily localized in the nucleus in most normal tissues examined, except in the bladder, lung and pancreas-the latter two being secretory organs. Cytoplasmic localization of METTL3 has also been documented in other cancers, including lung cancer, chronic myeloid leukemia, and gastric cancer, where cytoplasmic METTL3 promotes translation independently of its catalytic activity[6–8,38]. However, its function in non-malignant cells remains poorly understood. Could the cytoplasmic redistribution of METTL3 in secretory organs be linked to exocytosis?

Aberrant protein localization is a well-established mechanism by which cancer cells promote transformation, survival, proliferation, and resistance to anti-neoplastic therapies[39]. Recent studies have shown that acetylation of METTL3 facilitates its translocation to the cytoplasm and suppresses its chromatin binding[40–42]. Beyond classical acetyltransferases such as p300, METTL3 acetylation is enhanced by the kinase PAK2, revealing a sophisticated crosstalk between phosphorylation and acetylation[42]. Notably, PAK2 inhibition promotes ferroptosis, a form of programmed cell death driven by iron-dependent lipid peroxidation, and enhances cisplatin

efficacy, in a manner dependent on METTL3 acetylation and its dissociation from chromatin[42]. It would be of interest to determine whether the resulting effects on ferroptosis are not solely due to reduced m^6A modification of enhancer RNAs and pRNAs, which stabilizes anti-ferroptotic transcripts, but also from impaired cytoplasmic localization of METTL3. Such insights could uncover previously unrecognized, methylation-independent functions of cytoplasmic METTL3 and suggest novel therapeutic strategies by co-targeting METTL3 localization and ferroptosis pathways.

Our study uncovers a distinct cytoplasmic role for METTL3, expanding beyond its previously characterized function in translation. We have identified METTL3 as a novel interacting partner of the exocyst complex, a key player in exocytosis by tethering secretory vesicles to the plasma membrane prior to fusion[10,13]. Given the established role of EXOC7 in breast tumorigenesis and its association with metastatic outcomes in TNBC[16,43], we further characterized its interaction with METTL3, although we cannot exclude the possibility that METTL3 may mediate exocyst function through interactions with additional members of the complex retrieved in mass spectrometry analysis. Notably, METTL3–EXOC7 interaction occurs independently of METTL14, indicating that METTL3's m^6A methyltransferase activity is not required for binding EXOC7. Since METTL3 acetylation disrupts its interaction with METTL14[42], it is plausible that the acetylated form of METTL3 constitutes the pool that interacts with EXOC7.

EXOC7 undergoes isoform switching in breast cancer[12], a process that we demonstrate is regulated by m^6A mRNA modification. Additionally, METTL3 stabilizes EXOC7 protein levels, particularly the long isoform. This scaffolding role of METTL3 in stabilizing its binding partners through m^6A-independent mechanisms has also been observed for other proteins, such as METTL14, WTAP, and p53[23,24,44]. Reduced levels of EXOC7 upon METTL3 knockdown impaired exocyst complex assembly, leading to defective vesicle trafficking, a defect that is not observed with catalytic inhibition, further supporting a non-enzymatic role of METTL3 in this process. Our proteomics data align with these findings, revealing that METTL3 knockdown, but not catalytic inhibition, reduces the breast cancer secretome, particularly among proteins that are reliant on EXOC7. Previous studies have shown that METTL3 and METTL14 can transcriptionally regulate the senescence-associated secretory phenotype independently of m^6A[44]. Whether this holds true in breast cancer remains to be explored. Importantly, proteins diminished

in the secretome upon METTL3 silencing are enriched in pathways critical for cancer progression, including ECM organization, cell adhesion, and metastasis. Functionally, METTL3 silencing, without inhibiting its enzymatic activity, impairs invadopodia formation and affects collagen-rich ECM and FA architecture.

While METTL3 inhibitors are in clinical trials for advanced cancers[45], evidence shows its catalytic activity is dispensable for pro-tumorigenic functions like translation in lung and gastric cancers[7,8]. Our findings further demonstrate that the methyltransferase activity of METTL3 is not required for its function in exocytosis. Thus, approaches such as PROTAC-mediated degradation [46], which target METTL3 for proteolysis, may offer a more effective approach in contexts where cytoplasmic METTL3 drives oncogenic traits through non-catalytic mechanisms.

A key open question remains: Why is METTL3 involved in vesicle trafficking? While our findings indicate that the METTL3-EXOC7 interaction is RNA-independent, it is unclear whether these intracellular vesicles carry RNAs destined for secretion to the ECM or plasma membrane. One possibility is that METTL3 functions as a reader, binding to a specific subset of RNAs while simultaneously interacting with the exocyst complex, thereby ensuring the efficient export of these RNAs.

The presence of extracellular mRNAs within extracellular vesicles (EVs) has been well-documented[47–49]. EV-derived mRNAs can be transferred to recipient cells, where they are translated into functional proteins, serving as key mediators of intercellular communication. However, the role of naked, non-vesicular extracellular RNA (exRNA) remains largely unexplored. Beyond their potential in intercellular communication, non-vesicular exRNAs may contribute to RNA homeostasis by balancing synthesis, degradation, excretion, and reuptake. Additionally, rapid clearance of specific RNAs may function as a molecular switch in cellular gene expression programs in response to external stimuli. Furthermore, degradation byproducts of extracellular RNAs, akin to protein degradation products, could be recycled to fuel cellular metabolism[50].

We propose that, in addition to being secreted, these vesicles may carry RNAs that associate with the plasma membrane. RNA-membrane interactions are known to play functional roles in cellular processes[51,52]. For instance, lncRNA LINK-A is enriched in lipid-rich domains in TNBC tissues,

where it interacts with Phosphatidylinositol-3,4,5-trisphosphate (PI(3,4,5)P3) to recruit and activate AKT[53]. Ribosomal proteins also accumulate at specific plasma membrane regions, where they are released and recruited to translation hotspots in response to external stimuli. This mechanism supports actin filament remodeling and cell surface plasticity, which are important for maintaining a mesenchymal-like morphology in TNBC cells[54–56]. Hence, we argue that vesicle trafficking mechanisms may be more complex than previously thought, potentially involving RNA release. However, due to challenges in purifying intracellular vesicles, further investigation is needed.

Overall, our study provides novel insights into the role of METTL3 in exocytosis and its broader contribution to breast cancer. Targeting both the catalytic and non-catalytic functions of METTL3 could offer new avenues for diagnosis and treatment in breast cancer and other malignancies. Further investigations are warranted to unravel the complex interplay between the m^6A-dependent and m^6A-independent roles of METTL3 and to identify the mechanisms that govern its function in tumorigenesis.

Methods

Antibodies

The following antibodies were purchased from the indicated suppliers. For western blot: anti-βACTIN (Sigma, A5441, 1:5,000), anti-METTL3 (Abcam, ab221795, 1:2,000), anti-METTL14 (Sigma, HPA038002, 1:4,000), anti-EXOC7 (Abcam, ab118792, 1:2,000), anti-EXOC5 (Santa Cruz Biotechnology, sc514802, 1:500), anti-EXOC8 (Abcam, ab254804, 1:2,000), anti-Flag (Sigma, F3165, 1:3,000), anti-GAPDH (Invitrogen, PA1-987, 1:2,000), anti-lamin A+C (Abcam, ab108992, 1:2,000), anti-H3 (Abcam, ab8895, 1:8,000), anti-MMP1 (R&D Systems, MAB901-SP, 1:1000), anti-RPL22 (Proteintech, 25002-1AP, 1:2,000), Goat Anti-Mouse IgG H&L (HRP) (Abcam, ab6789, 1:10,000), Goat Anti-Rabbit IgG H&L (HRP) (Abcam, ab6721, 1:10,000). For co-immunoprecipitation experiments: anti-METTL3 (Bethyl, A301-567A, 3 µg), anti-EXOC7 (Abcam, ab118792, 3 µg), anti-Flag (Sigma, F3165, 3µg), anti-METTL14 (Sigma, HPA038002, 3 µg). For IF staining: anti-METTL3 (Bethyl, A301-567A, 1:100), anti-EXOC7 (Santa Cruz Biotechnology, sc-365825, 1:50), anti-Flag (Sigma, F3165, 1:100), anti-VSVG (Kerafast, EB0010, 1:100), Phalloidin-iFluor 594 Reagent (Abcam, ab176757, 1:1,000), Phalloidin-iFluor

488 Reagent (Abcam, ab176753, 1:1,000) Alexa Fluor™ 488 goat anti-mouse IgG (H+L) (Invitrogen, A11029, 1:1,000). Alexa Fluor™ 568 goat anti-Mouse IgG (H+L) (Invitrogen, A110231, 1:1,000), Alexa Fluor™ 568 goat anti-rabbit IgG (H+L) (Invitrogen, A11011, 1:1,000). For IHC stainings: anti-METTL3 (Abcam, ab221795, 1:200), anti-Ki67 (Abcam, ab16667, 1:100).

Constructs and cloning strategy

To reconstitute METTL3 expression in MDA-MB-231, the cDNA of human *METTL3* was amplified with RevertAid First Strand cDNA Synthesis Kit and cloned into the doxycycline inducible pInducer20 lentivector (Addgene #44012), using Esp3I and XhoI as restriction enzymes. A nuclear export signal (NES) was added at the 3'end to enrich the expression of METTL3 to the cytoplasm. Silenced point mutations were generated at the shRNA2 targeting site to allow the inducible expression of METTL3. To produce catalytically dead METTL3, point mutations were generated at the catalytic site (DPPW ⟶ APPA). Additionally, to produce METTL3 lacking the LH domain, the N-terminal 1–34 amino acids were deleted.

To evaluate the interaction between METTL3 and EXOC7 in vitro, Flag tag and MYC-tag constructs were generated. Briefly, the cDNA of human METTL3 was amplified and cloned into pGEX6P-2 vector using BamHI and SalI as restriction enzymes, to further produce and purify GST-tagged METTL3 proteins in bacteria. The cDNA of human EXOC7 isoform 1 was amplified and cloned into pET22b vector using NdeI and EcoRI as restriction enzymes.

For EXOC7 overexpression and TNT formation assay, EXOC7 short (isoform 2) and long (isoform 6) isoforms were cloned into pEGFP-C3-EXO70 vector (Addgene #53761). First, the isoform 1 was removed by digesting the vector using BamHI and XhoI as restriction enzymes. The cDNA of EXOC7 isoforms 2 and 6 was amplified with RevertAid First Strand cDNA Synthesis Kit and cloned into the pEGFP-C3 empty vector using the restriction enzymes. To perform overexpression experiments followed by gelatin degradation assays, EXOC7 isoforms were cloned into pCDNA3 vector. pEGFP-C3-EXOC7-isoform2 and pEGFP-C3-EXOC7-isoform6 were used as a template to amplify the CDS of each isoform. Oligos used for the amplification contained a TCC sequence upstream followed by the restriction sites (BamHI for the forward primer and XhoI for the reverse). Both pCDNA3 and amplified isoforms were double digested with BamHI and XhoI, which were next ligated overnight at 16 ºC.

All constructs generated were confirmed by Sanger sequencing. All primers used for cloning purposes are described in Suppl. Table 3.

Primers

All primers used in this study are listed in the Suppl. Table 3.

Cell culture

MCF7, MDA-MB-231, U2OS and HEK293T cell lines were cultured in Dulbecco's Modified Eagle Medium (DMEM; Gibco) supplemented with 10% fetal bovine serum (Gibco) and 1% penicillin/streptomycin (Gibco). For MCF7 and MDA-MB-231 media was additionally supplemented with 10 μg ml^{-1} insulin (Sigma-Aldrich). MCF10-A and hTERT-HME1 cell lines were cultured in DMEM/F12 (Sigma-Aldrich) supplemented with 5% heat-inactivated horse serum (Gibco), 20 ng ml^{-1} epidermal growth factor (EGF; Sigma-Aldrich), 0.5 mg ml^{-1} hydrocortisone (Sigma-Aldrich), 100 ng ml^{-1} cholera toxin (Sigma-Aldrich), 10 μg ml^{-1} insulin (Sigma-Aldrich), and 1% penicillin/streptomycin (Gibco). OVCAR-8 cell lines were cultured in RPMI 1640 medium (Gibco) supplemented with 10% fetal bovine serum (Gibco) and 1% penicillin/streptomycin (Gibco). CCE murine ESCs were culture and maintained on 0.1% gelatin-coated tissue culture plates under feeder-free culture conditions. The complete media composition consists of Dulbecco's modified Eagle's medium (DMEM; Gibco) 15% fetal bovine serum (Gibco), 1% MEM non-essential amino acids (Sigma-Aldrich), 0.1 mM of β-mercaptoethanol, 1% L-glutamine (Hyclone) and 1% penicillin/streptomycin (Gibco). Complete media was supplemented with 0.01 ng μl^{-1} Leukemia inhibitory factor (LIF; R&D systems). All cell lines were cultured at 37 °C under 5% CO_2 in a humidified incubator.

Generation of knockdown cell lines

For lentivirus production, pLKO.1-shRNAs, the packaging vector pCMV-dR8.2 dvpr and the envelope vector pCMV-VSV-G (ratio 6:8:2) were co-transfected into HEK293T cells using Jet-PEI Polyplus following the manufacturer's instructions. Culture media containing the lentiviral particles was collected after 48 and 72 h, filtered through a 0.45 μm filter and concentrated using Amicon Ultra-15 Centrifugal Filter (Merck). Cells were transduced with lentiviral supernatant and Polybrene (8 μg ml^{-1}). After 2 days, infected cells were selected with puromycin (1 μg ml^{-1}) for 4

days. The efficiency of METTL3 knockdown was evaluated by western blot analysis. The shRNA sequences are listed in Supplementary Table 3.

Generation and induction of METTL3-cyto, METTL3-cyto_mut and ΔLH-METTL3 stable cell lines in MDA-MB-231

To reintroduce METTL3-cyto, METTL3-cyto_mut and ΔLH-METTL3, stable MDA-MB-231 cell lines were generated by lentiviral infection followed by selection with neomycin (8 mg ml^{-1}) for 8 days. After selection, exogenous METTL3 expression was induced with doxycycline (1 μg ml^{-1}) for 9 days. On day 9 of induction, non-induced cells were seeded for subsequent lentiviral infection with either a scramble control or METTL3 knockdown (sh2). Doxycycline-induced cells were infected with lentiviral particles targeting METTL3 (sh2 + dox, rescue). After 2 days, cells were selected with puromycin (1 μg ml^{-1}) for 4 days. The efficiency of METTL3 knockdown and rescue was confirmed by western blot analysis. All downstream experiments were conducted after 4 days of puromycin selection.

RNA extraction and RT–qPCR

Total RNA was extracted using the RNeasy Mini Kit (Qiagen) following the manufacturer's instructions. 1 μg of total RNA was reverse transcribed using RevertAid First Strand cDNA Synthesis kit (Invitrogen) and quantitative PCR was performed using Power Up SYBR master mix (Applied Biosystems) on Quantstudio Flex6 instrument. *βACTIN* was used for normalization.

RT–PCR

1 μg of total RNA was reverse transcribed using the RevertAid First Strand cDNA Synthesis kit (Invitrogen). PCR was performed using the DreamTaq Green Master mix (Thermo Fisher Scientific) with specific primers to amplify the different splicing isoforms of *EXOC7*.

mRNA purification

mRNAs were purified using Dynabeads following the manufacturer's recommendations. mRNAs were eluted twice with RNase-free water.

mRNA mass spectrometry analysis

The RNAs were hydrolyzed to ribonucleosides by 20 U Benzonase® Nuclease (Santa Cruz Biotech, cat. no. sc-202391) and 0.2 U Nuclease P1 (Sigma, cat. no. N8630-1VL) in 10 mM ammonium acetate pH 6.0 and 1 mM magnesium chloride at 40 °C for 1 h. After that, ammonium bicarbonate to 50 mM, 0.002 U phosphodiesterase I and 0.1 U alkaline phosphatase (Sigma) were added, and incubated further at 37 °C for 1 h. The hydrolysates were mixed with 3 volumes of acetonitrile and centrifuged (16,000 x g, 30 min, 4 °C). The supernatants were dried and dissolved in 50 µl water for LC-MS/MS analysis of modified and unmodified ribonucleosides. Chromatographic separation was performed using an Agilent 1290 Infinity II UHPLC system with an ZORBAX RRHD Eclipse Plus C18 150 × 2.1 mm ID (1.8 µm) column protected with an ZORBAX RRHD Eclipse Plus C18 5 × 2.1 mm ID (1.8 µm) guard column (Agilent). The mobile phase consisted of water and methanol (both added 0.1% formic acid) run at 0.23 mL/min. For modifications, starting with 5% methanol for 0.5 min followed by a 2.5 min gradient of 5%–15% methanol, a 3 min gradient of 15%–95% methanol and 4 min re-equilibration with 5% methanol. A portion of each sample was diluted for the analysis of unmodified ribonucleosides which was chromatographed isocratically with 20% methanol. Mass spectrometric detection was performed using an Agilent 6495 Triple Quadrupole system, monitoring the mass transitions 268.1-136.1 (A) and 282.1-150.1 (m^6A) in positive electrospray ionization mode.

Whole-cell protein extraction

Cells were washed in cold PBS, pelleted, and lysed with ice-cold lysis buffer (50 mM HEPES pH 7.5, 150 mM NaCl, 3 mM $MgCl_2$, 0.2% Triton X-100, 0.2% Nonidet NP-40, 10% glycerol) supplemented with protease inhibitor cocktail (Thermo Fisher Scientific) for 15 min on ice. Afterwards, lysates were sonicated (Bioruptor, Diagenode) for ten cycles with 30 s pulses on/off. Lysates were centrifuged at 13 300 rpm for 15 min, and supernatants were collected.

Nuclear and cytoplasmic extracts

For nuclear and cytoplasmic extraction not involving co-immunoprecipitation experiments, a homemade extraction kit was used. Briefly, cells were washed with PBS and harvested by trypsinization or by scraping. Cells were pelleted by centrifugation at 2,200 rpm for 5 min at 4 °C, then resuspended in at least 5 volumes of cold cytoplasmic extraction buffer (10 mM HEPES pH 8, 10 mM KCl, 2 mM $CaCl_2$, 0.34 M sucrose, 10% glycerol, 0.2% IGEPAL CA-630, 1X Protease

inhibitor cocktail). After vortexing, cells were incubated on ice for 10 min, followed by centrifugation at 8,000 rpm for 5 min at 4 °C. The supernatant was transferred to pre-kept as cytoplasmic extract.

CHX experiment

HEK293T cells were seeded at a density of 1.5 x10^6 in a 60 mm plate. After overnight incubation cells were treated with CHX at a final concentration of 100 µg/ml for 0, 24 and 48 h, respectively. RPL22 was used as a loading control since β-actin has a shorter half-life than 48 h.

Non-reducing PAGE

The cultured medium was removed, and cells were resuspended in 1X PBS and centrifuged at 500 x g for 5 min. The cell pellet was then resuspended in NP-40 lysis buffer containing 10 mM Tris-HCl (pH 7.5), 150 mM NaCl, 0.5 mM EDTA, and 0.5% Nonidet™ P40 substitute, supplemented with 1X Halt protease inhibitor. The cell suspension was gently mixed by pipetting up and down and incubated on ice for 20 min before centrifugation at 17,000 x g for 15 min at 4 °C. The supernatant was collected as the whole cell extract.

Protein samples for non-reducing western blot were prepared using 4X Laemmli buffer and separated on a 7.5% polyacrylamide gel without SDS. The running buffer contained 25 mM Tris, 192 mM glycine, and 0.1% SDS. Gels were run at 100V and transferred onto a nitrocellulose membrane at 80V for 2 h under cold conditions. The membranes were blocked with 5% milk in PBS containing 0.1% Tween-20 (PBS-T) prior to immunoblotting with the indicated primary and corresponding secondary antibodies.

Co-immunoprecipitation

Cytoplasmic extracts used for co-immunoprecipitation experiments were obtained using the NE-PER Nuclear and Cytoplasmic Extraction Reagents (Thermo Scientific). 500 µg of cytoplasmic extracts were pre-cleared with Pierce Protein G Agarose beads (Thermo Fisher) for 1 h at 4 °C and treated with rabbit IgG control or primary antibody (3 µg per immunoprecipitation) and incubated overnight at 4 °C. Next, washed Pierce Protein G Agarose beads (Thermo Fisher) were added, and the solution was incubated for additional 3 h with gentle rotation. Then, beads were washed four

times 5 min with ice-cold IP buffer (10 mM Tris pH 7.4, 1 mM EDTA, 1 mM EGTA pH 8, 150 mM NaCl, 1% Triton and 0.2 mM Sodium Orthovanadate, 1X Protease inhibitor cocktail). Immunoprecipitated complexes were eluted using reducing sample buffer and analyzed by immunoblotting.

Recombinant protein purification, *in vitro* transcription/translation and GST pull down

GST-tagged METTL3 proteins (full-length, N-terminal, methyltransferase, leader helix, or ZF domains) were purified from *Escherichia coli* strain Rosetta (DE3). Protein expression was induced overnight at 20 °C and cells were lysed by sonication and lysates were clarified by centrifugation and passed through a 0.45 µm filter. The lysates were incubated with Glutathione Sepharose 4B beads for 1.5 h at 4 °C. The resin was added to a gravity flow column and GST-tagged proteins were eluted with reduced L-Glutathione in elution buffer (125 mM Tris-Cl 8.0, 150 mM NaCl) after washing (125 mM Tris-Cl pH 8.0, 150 mM NaCl). GST-tagged proteins were stored in NETN buffer (20 mM Tris-Cl pH 8.0, 100 mM NaCl, 0.5 mM EDTA, 0.5% NP-40) and analyzed by SDS-PAGE followed by Coomassie blue staining.

In vitro transcription and translation for MYC-tagged EXOC7 was performed by incorporating biotinylated lysine to the translation reaction as a precharged epsilon-labeled biotinylated lysine-tRNA complex using Transcend Non-Radioactive Translation Detection systems (Promega). Briefly, 1 µg of pET22b -MYC-EXOC7 was incubated with TNT quick master mix and 1 µl methionine at 30 °C for 90 min.

To perform GST pull-down assay, MYC-EXOC7 protein and affinity purified GST-tagged METTL3 proteins were mixed in a ratio of 2.5:1 and incubated at 4 °C for 3 h. Then, equilibrated glutathione beads were added to this mixture and incubated at 4 °C for 2 h with gentle shaking. The protein complex was washed three times with NETN buffer (100 mM NaCl, 20 mM Tris-Cl pH 8.0, 0.5 mM EDTA and 0.5% (v/v) NP-40) and eluted with a loading buffer. Immunoprecipitated complexes were resolved by SDS-PAGE, transferred to PVDF membranes (Invitrogen), and detected with Streptavidin-HRP conjugate. For GST detection, the PVDF membranes were washed three times with PBST and incubated with 0.1% Ponceau red in acetic acid.

Nuclei pellets were then resuspended in 2.5 volumes of RIPA buffer (50 mM Tris pH 7.5, 100 mM NaCl, 3 mM EDTA, 0.5% IGEPAL CA-630, 1X Protease inhibitor cocktail). Samples were rotated for 15 min at 4 °C and sonicated for 10 cycles of 30 s on/off. Following centrifugation at maximum speed for 30 min at 4 °C, supernatant was collected and kept as the nuclear extract.

Wound healing assay

2 x 10^5 cells were seeded in a 12-well plate, and after 24 h cells were scratched to create a wound. After 24 and 48 h, pictures were taken, and the wound area was measured to assess cell migration. When STM2457 was used, the inhibitor was added when just after scratching at a final concentration of 5 µM.

Cell proliferation

1 x 10^5 cells were seeded in 6-well plate and were counted using trypan-blue (Bio-Rad) every second day for 6 days. When STM2457 was used, the inhibitor was added when seeding at a final concentration of 5 µM.

Immunofluorescence staining

Cells were fixed with 4% paraformaldehyde (Sigma-Aldrich) at room temperature (RT) for 15 min, washed three times, permeabilized for 30 min with 0.25% Triton-X-100 (Sigma-Aldrich) in PBS, and washed three times with PBS and blocked with 10% goat serum (Invitrogen) and bovine serum albumin (Hyclone) for 1 h. Cells were incubated with primary antibodies overnight at 4 °C and washed four times with PBS. Cells were incubated with secondary antibodies at RT. DAPI was used for nuclei staining. Imaging was acquired using Zeiss 710 and Leica SP8 X confocal microscope.

Vesicle trafficking

Vesicle trafficking assays using GFP-VSV-G^{ts045} mutant were performed as described previously[25,57]. Briefly, cells were transfected with 1.5 µg of the VSV-G^{ts045}-pEGFP-N1 vector using Lipofectamine™ LTX Reagent (Invitrogen). Cells were immediately placed at 40 ºC, a restrictive temperature where the VSV-G mutant is misfolded and retained within the ER. Next, after overnight incubation, cells were shifted to 20 ºC for 2 h for Golgi arrest and then moved at

32 ºC and left for 1 and 3 h in the presence of 100 µg/ml of cycloheximide (Sigma) to block protein synthesis. For each time point, cells were washed with PBS, fixed with 4% paraformaldehyde (PFA, Sigma-Aldrich) at RT for 15 min, washed and blocked for 15 min with blocking solution (1% bovine serum albumin, 10% goat serum). The coverslips were then incubated with the 8G5 monoclonal antibody against the extracellular domain of VSV-G (EB0010, Kerafast). No detergent was used in the immunofluorescence procedure. The amount of VSV-G fused to the plasma membrane was normalized to the total amount of VSV-G in the cells. For experiments performed using METTL3 inhibitor, cells were treated with 5 µM STM2457 for 48 h before seeding. STM2457 concentration was maintained throughout the experiment.

Tunneling nanotube assay

8 x 10^4 MDA-MB-231 cells were seeded in a 12-well plate. After overnight incubation, cells were transfected with 1 µg of plasmid (pEGFP, pEGFP-C3-EXOC7-short or pEGFP-C3-EXOC7-long) using Lipofectamine™ LTX reagent (Invitrogen). Images were captured 24 h after transfection using a Nikon ECLIPSE Ts2 inverted microscope coupled to a DMK NME33UX174 camera. TNT length was evaluated using ImageJ. When two cells were connected by a TNT, the total length of the projection was divided by two. For METTL3 silencing TNT experiments, MDA-MB-231 cells were treated with small interfering RNA (siRNA) targeting METTL3 or siRNA control for 72 h prior to TNT assay. For experiments with METTL3 inhibitor, cells were treated with 10 µM STM2457 for 48 h before seeding. STM2457 concentration was maintained throughout the experiment.

Invadopodia formation assays

Invadopodia formation analyses were performed as previously described [33]. Briefly, coverslips were coated with poly-L-lysine (50 µg ml^{-1}) for 20 min at 37 °C, crosslinked with 0.5% glutaraldehyde for 15 min at RT. After washing three times with PBS, coverslips were inverted on a 40 µl drop of 1 mg ml^{-1}green 488-labeled gelatin (Sigma-Aldrich) for 20 min at RT. Coverslips were then carefully washed with PBS and incubated with 5 mg ml^{-1} of sodium borohydride to quench auto-fluorescence. Coverslips were incubated at least 1 h at 37 °C with complete medium before seeding. 1 x 10^5 cells were seeded per coverslip and incubated 6 h at 37 °C. For METTL3 knockdowns, cells were seeded after 4 days of puromycin selection, while for METTL3 inhibitor

after 48 h of treatment in the presence of 5 μM STM2457. Cells were fixed with 4% paraformaldehyde (Sigma-Aldrich) at RT for 15 min, washed three times with PBS, stained with Phalloidin-iFluor 594 (Invitrogen) and mounted on slides. Images were acquired using Leica SP8 X confocal microscope. Fluorescent gelatin degradation was quantified performed using ImageJ.

Focal adhesions sample preparation

Coverslips were coated with 10 μg ml^{-1} PureCol® (Advanced Biomatrix) for 20 min at 37 °C, washed with PBS, and blocked with 2% BSA in PBS for 1 h at 37 °C. After blocking, coverslips were washed twice with PBS, and 100,000 cells were seeded per condition and allowed to attach for 24 h. Following incubation, cells were washed twice with PBS and fixed with 4% PFA in cytoskeletal buffer (0.1 M MES at pH 6.1, 1.38M KCl, 30 mM MgCl2, 20 mM EGTA) for 20 min at 37 °C. Cells were then incubated with Triton buffer (0.5% Triton in cytoskeletal buffer) at RT for 5 min, followed by incubation in glycine buffer (0.1M Glycine in cytoskeletal buffer) for 10 min at RT with gentle rocking.

Subsequently, cells were washed three times with TBS (10 min per wash) and blocked with BTT buffer (4% w/v BSA, 0.1% v/v Tween-20 in 1X TBS) for 1 h at RT. Coverslips were incubated overnight at 4 °C with a primary antibody against Paxillin, diluted in BTT. The following day, cells were washed three times with TBS (10 min per wash) and incubated for 1 h at RT with a secondary antibody and phalloidin marker, diluted in BTT. Coverslips were then rinsed once with PBS and incubated for 5 min with 300 nM DAPI in PBS. Finally, coverslips were washed three times with TBS-T (0.1% v/v Tween-20 in 1X TBS) for 5 min each and stored in TBS at 4 °C until imaging.

Total internal reflection microscopy (TIRFM)

The stained cells were imaged on an inverted Nikon Eclipse Ti-E2 microscope equipped with an Apo TIRF 60X oil-immersion objective (NA=1.49). TIRF images were acquired with laser excitation using the Ti-2 Lapp laser system with 488 nm and 561 nm wavelength. Epi fluorescence was acquired using a Spectra light source with 365 nm, 488 nm and 561 nm respectively. Images of the same cell were acquired in all 3 settings with 100ms exposure (TIRF 488, TIRF 561, Epi 365). For signal detection a Prime 95B sCMOS camera was used.

Image analysis for focal adhesion quantification

Subsequent to image acquisition, the paxillin channel (TIRF 488) was used for quantification of focal adhesion morphology using the focal adhesion analysis server (FAAS)[58]. A detection threshold of 4 and a minimum adhesion size of 4 pixels were used for all conditions. FA area and length for every 10 focal adhesions within a cell was then calculated and plotted as previously described[59].

3D invasion assay

The assay was conducted by initiating cell aggregation under different conditions. Briefly, 5000 cells (DMSO/ STM2457-treated and knockdown conditions) were seeded into low-attachment, U-bottom 96-well plates coated with 1% agarose. To initiate aggregation, the plates were centrifuged at 200 x g for 5 min, after which the cells were incubated for 5 days to form compact aggregates. On the same day, to assay collagenase activity, the aggregates in each well were embedded in a cold mixture of Matrigel ® Matrix (11573620, Fisher Scientific), 775 µg/ml PureCol ® (Advanced Biomatrix), and DPBS that was mixed in 2:1:1 ratio. The plates were then briefly centrifuged at 200 x g and incubated at 37 °C and 5% CO_2 to initiate Matrigel polymerization. Bright-field images were captured on day 0 and subsequently at 24 h and 96 h post-treatment. Image analysis was conducted using ImageJ software. Spheroid invasion and growth were quantified by measuring the area in bright-field images using a combination of thresholding, the magic wand tool, and the measurement tool, or manually using the freehand tool.

Animal study

Female BALB/c nude mice (4 weeks old) were used in this study. For the tumor formation analysis, control and METTL3 knockdown MDA-MB-231 cells were injected into the mammary fat pad of mice. Mice weight was recorded every week until the day of sacrifice. Mice were sacrificed at day 21 and tumors were extracted. Tumor weight and volume were measured. For the metastasis xenograft model, MDA-MB-231 cells knockdown of *METTL3* expressing luciferase were injected in the mice tail vein. The metastatic spreading was monitored by bioluminescence on day 55. The mouse experiments were approved by the Ethical Committee for Animal Experimentation of the

Catalan Government (project number #10568) were conducted in compliance with the guidelines for animal experimentation at IDIBELL, Universitat de Barcelona.

Tissue staining and immunohistochemistry

Thin sections of formalin-fixed paraffin embedded tissues were deparaffinized, rehydrated and rinsed with water, and sections were mounted on slides. For H&E staining, hematoxylin and 0.5% eosin were used. For IHC, Ki67 and METTL3 antibodies were used. Staining intensity is recorded manually using the H-scoring system.

TMA

Breast cancer tissue and multi normal human TMAs were purchased from US biomax (BC081116c and FDA999y) and stained as previously described in the above section. Staining intensity is recorded manually using the H-scoring system.

H-score

Staining was quantified using an H-scoring system based on the percentage of tumor epithelial cells stained: [1 × (% cells 1+) + 2 × (% cells 2+) + 3 × (% cells 3+)]. The final score ranges from 0 to 300. Nuclear and cytoplasmic scorings were analyzed separately for the TMAs.

Mass spectrometry analysis to identify METTL3 interacting proteins

500 µg of cytoplasmic extracts were pre-cleared with protein G magnetic beads (Bio-Rad) for 1 h at 4 °C then incubated overnight on a rotation with 3 µg of METTL3 antibody at 4 °C. Protein G magnetic beads were added to the samples and incubated for 3 h at 4 °C with gentle rotation. Beads were washed four times with ice-cold immunoprecipitation buffer (10 mM Tris pH 7.4, 1 mM EDTA, 1 mM EGTA pH 8.0, 150 mM NaCl, 1% Triton and 0.2 mM Sodium Orthovanadate). Immunoprecipitated complexes were eluted with 5X reducing sample buffer. Following elution, immunoprecipitated complexes were mixed with 2 µl of 40% acrylamide solution for 20 min and resolved by SDS-PAGE. Gels were then stained with Coomassie blue (Thermo Fisher Scientific) and sent to the Research core unit proteomics, Medizinische Hohschule Hannover for mass-spectrometry. Briefly, gels were cut in slices, digested with trypsin, peptides were extracted and subjected to LC-MS analysis. Proteins were identified using MaxQuant Andromeda and human

entries of Uniprot database (FDR < 0.01). Proteins quantified in at least three out of the four biological replicates were used. Missing values were imputed from a normal distribution with a down shift $\log_2$ of 1.8, and width 0.3. Significantly enriched proteins were identified using *t*-test; the enrichment threshold was Log2FC >1.

Secretome analysis

After 4 days of puromycin selection for METTL3 and EXOC7 knockdown MDA-MB-231 cells or 48 h in the presence of 5 µM STM2457, two million MDA-MB-231 cells were seeded in a TC100 dish using complete DMEM media. The following day, the media was removed, and cells were washed two times with PBS (one quick wash and a second one for 2 min at RT) and incubated with 5 ml of FBS- and phenol red-free DMEM for 16 h. Afterwards, media was collected and filtered through a 0.45 µm filter and concentrated down to 300 µl using a 3 kDa Vivaspin™ 6 Columns (Cytiva) at 4 000 g and 4 °C for 90 min. Samples were digested with a modified sp3 protocol, as previously described[60,61]. Briefly, samples were added to a bead suspension (10 µg of beads (Sera-Mag Speed Beads, 4515-2105-050250, 6515-2105-050250) in 10 µl 15% formic acid and 30 µl ethanol) and incubated shaking for 15 min at RT. Beads were then washed four times with 70% ethanol. Proteins were digested overnight by adding 40 µl of 5 mM chloroacetamide, 1.25 mM TCEP, and 200 ng trypsin in 100 mM HEPES pH 8.5. Peptides were eluted from the beads and dried under a vacuum. Peptides were then labelled with TMT10plex (knockdown experiment) or TMTpro (STM2457 experiment) (Thermo Fisher Scientific), pooled and desalted with solid-phase extraction using a Waters OASIS HLB Elution Plate (30 µm). Samples were fractionated onto 48 fractions on a reversed-phase C18 system running under high pH conditions, pooling every twelve fractions together. Samples were analyzed by LC-MS/MS using a data dependent acquisition strategy on a Thermo Fisher Scientific Vanquish Neo LC coupled with a Thermo Fisher Scientific Orbitrap Exploris 480. Raw files were processed with MSFragger[62] against a Homo sapiens FASTA database downloaded from UniProt (UP000005640) using standard settings for TMT. Protein hits were filtered using a custom R script to select proteins with a signal peptide without a transmembrane domain according to Uniprot database, as previously described[11]. Data were normalized using vsn[63], and statistical significance was determined using limma[64] considering significant proteins as those with a log2 fold-change <- 0.585 or log2 fold-change >0.585 and p-value < 0.05.

Gene ontology (GO) analysis

Gene ontology (GO) analysis was performed using the web tool The Database for Annotation, Visualization and Integrated Discovery (DAVID) (http://david.abcc.ncifcrf.gov/).

Statistical analysis

Data are shown as mean ± s.d. GraphPad Prism 8.0.0 for Windows was used to perform the statistical analysis (GraphPad Software). The significance was determined using Student's *t*-test, and two-Way ANOVA with Dunnett's correction for multiple comparison

Data availability

The mass spectrometry proteomics data have been deposited to the ProteomeXchange Consortium via the PRIDE partner repository with the dataset identifier PXD062959.

Acknowledgements

The authors thank members of the Aguilo laboratory for useful discussion; the Biochemical Imaging Centre Umeå; M. Lindberg for assisting with the cloning; S. Gildlund for performing IHC staining; and N. Nakamura for his generous gift of GFP-VSV-Gts045 plasmid. This research was supported by grants from the Knut and Alice Wallenberg Foundation, Umeå University, Västerbotten County Council, Swedish Research Council (2017-01636; 2022-01322), Kempe Foundation (SMK-1766), and Cancerfonden (190337 Pj; 22 2455 Pj). M.E.-S. is part of the ROPES ITN, which received funding from the European Union's Horizon 2020 research and innovation program under the Marie Sklodowska-Curie grant agreement number 956810. Mass spectrometry-based proteomics was enabled by a grant from the Kempe Foundation (JCK3126).

Author contributions

F.A. conceived and designed the study. M.E.-S., D.P.B., C.A., P.B. G.F., S.M. performed experiments. R.R.-B. performed in vivo studies. K.S., H.P. and M.B. performed total internal reflection fluorescence microscopy. E.L. performed immunochemistry of TMAs, and A.M., S.Z.

and A.P. performed proteomics analysis. V.S. performed the analysis of focal adhesions. C.B.V. performed m^6A quantification from mRNA using LC–MS/MS. M.E.-S., C.A. and F.A. wrote the manuscript. All authors reviewed and edited the manuscript. F.A. supervised the study.

Competing interests

The authors declare no competing interests.

Supplementary data index:

- **Figure S1.** METTL3 promotes the formation of lung metastasis in mice, related to Figure 1.
- **Figure S2.** METTL3 localizes in both nuclei and cytoplasm of cell lines, related to Figure 2.
- **Figure S3.** METTL3 cytoplasmic interactome and subcellular fractionation, related to Figure 3.
- **Figure S4.** Characterization of EXOC7 alternative splicing isoforms in breast cancer cells and STM2457 characterization in MDA-MB-231, related to Figure 4.
- **Figure S5.** Characterization of EXOC7 overexpression in breast cancer cells, related to Figure 4.
- **Figure S6.** METTL3 modulates vesicle trafficking and the secretome, related to Figure 5.
- **Figure S7.** METTL3 rescue strategy and experiments, related to Figure 6.
- **Figure S8.** Effect of EXOC7 overexpression in invadopodia formation of MDA-MB-231 cells, related to Figure 6.
- **Figure S9.** Effect of EXOC7 overexpression in TNTs of MDA-MB-231 cells, related to Figure 6.

Supplementary Tables provided as Excel spreadsheets:

- **Supplementary Table 1.** Mass spectrometry of METTL3-interacting proteins. Number of unique peptides, sequence coverage, p-value, name, and accession number are indicated.
- **Supplementary Table 2.** Mass spectrometry of secretome analysis. Comparison type, UniProt ID, gene names, description, Log2FC and FDR are indicated.

Supplementary Tables provided in Word document:

- **Supplementary Table 3.** Primers, shRNAs and gRNAs used in this study.

References

1. He, P.C., and He, C. (2021). m ^{6} A RNA methylation: from mechanisms to therapeutic potential. EMBO J *40*. https://doi.org/10.15252/embj.2020105977.
2. Liu, J., Yue, Y., Han, D., Wang, X., Fu, Y., Zhang, L., Jia, G., Yu, M., Lu, Z., Deng, X., et al. (2014). A METTL3–METTL14 complex mediates mammalian nuclear RNA N6-adenosine methylation. Nat Chem Biol *10*, 93–95. https://doi.org/10.1038/nchembio.1432.
3. Malla, S., Melguizo-Sanchis, D., and Aguilo, F. (2019). Steering pluripotency and differentiation with N6-methyladenosine RNA modification. Biochimica et Biophysica Acta (BBA) - Gene Regulatory Mechanisms *1862*, 394–402. https://doi.org/10.1016/j.bbagrm.2018.10.013.
4. Destefanis, E., Avşar, G., Groza, P., Romitelli, A., Torrini, S., Pir, P., Conticello, S.G., Aguilo, F., and Dassi, E. (2021). A mark of disease: how mRNA modifications shape genetic and acquired pathologies. RNA *27*, 367–389. https://doi.org/10.1261/rna.077271.120.
5. Choe, J., Lin, S., Zhang, W., Liu, Q., Wang, L., Ramirez-Moya, J., Du, P., Kim, W., Tang, S., Sliz, P., et al. (2018). mRNA circularization by METTL3–eIF3h enhances translation and promotes oncogenesis. Nature *561*, 556–560. https://doi.org/10.1038/s41586-018-0538-8.
6. Ianniello, Z., Sorci, M., Ceci Ginistrelli, L., Iaiza, A., Marchioni, M., Tito, C., Capuano, E., Masciarelli, S., Ottone, T., Attrotto, C., et al. (2021). New insight into the catalytic -dependent and -independent roles of METTL3 in sustaining aberrant translation in chronic myeloid leukemia. Cell Death Dis *12*, 870. https://doi.org/10.1038/s41419-021-04169-7.
7. Lin, S., Choe, J., Du, P., Triboulet, R., and Gregory, R.I. (2016). The m 6 A Methyltransferase METTL3 Promotes Translation in Human Cancer Cells. Mol Cell *62*, 335–345. https://doi.org/10.1016/j.molcel.2016.03.021.
8. Wei, X., Huo, Y., Pi, J., Gao, Y., Rao, S., He, M., Wei, Q., Song, P., Chen, Y., Lu, D., et al. (2022). METTL3 preferentially enhances non-m6A translation of epigenetic factors and promotes tumourigenesis. Nat Cell Biol *24*, 1278–1290. https://doi.org/10.1038/s41556-022-00968-y.
9. Esteva-Socias, M., and Aguilo, F. (2024). METTL3 as a master regulator of translation in cancer: mechanisms and implications. NAR Cancer *6*, zcae009. https://doi.org/10.1093/narcan/zcae009.
10. TerBush, D.R., Maurice, T., Roth, D., and Novick, P. (1996). The Exocyst is a multiprotein complex required for exocytosis in Saccharomyces cerevisiae. EMBO J *15*, 6483–6494. https://doi.org/10.1002/j.1460-2075.1996.tb01039.x.
11. Pereira, C., Stalder, D., Anderson, G.S.F., Shun-Shion, A.S., Houghton, J., Antrobus, R., Chapman, M.A., Fazakerley, D.J., and Gershlick, D.C. (2023). The exocyst complex is an essential component of the mammalian constitutive secretory pathway. Journal of Cell Biology *222*. https://doi.org/10.1083/jcb.202205137.
12. Achour, C., Bhattarai, D.P., Groza, P., Román, Á.-C., and Aguilo, F. (2023). METTL3 regulates breast cancer-associated alternative splicing switches. Oncogene *42*, 911–925. https://doi.org/10.1038/s41388-023-02602-z.
13. Wu, B., and Guo, W. (2015). The Exocyst at a Glance. J Cell Sci. https://doi.org/10.1242/jcs.156398.

14. Mao, L., Zhan, Y., Wu, B., Yu, Q., Xu, L., Hong, X., Zhong, L., Mi, P., Xiao, L., Wang, X., et al. (2020). ULK1 phosphorylates Exo70 to suppress breast cancer metastasis. Nat Commun *11*, 117. https://doi.org/10.1038/s41467-019-13923-7.
15. Zuo, X., Zhang, J., Zhang, Y., Hsu, S.-C., Zhou, D., and Guo, W. (2006). Exo70 interacts with the Arp2/3 complex and regulates cell migration. Nat Cell Biol *8*, 1383–1388. https://doi.org/10.1038/ncb1505.
16. Lu, H., Liu, J., Liu, S., Zeng, J., Ding, D., Carstens, R.P., Cong, Y., Xu, X., and Guo, W. (2013). Exo70 Isoform Switching upon Epithelial-Mesenchymal Transition Mediates Cancer Cell Invasion. Dev Cell *27*, 560–573. https://doi.org/10.1016/j.devcel.2013.10.020.
17. Aguilo, F., Zhang, F., Sancho, A., Fidalgo, M., Di Cecilia, S., Vashisht, A., Lee, D.-F., Chen, C.-H., Rengasamy, M., Andino, B., et al. (2015). Coordination of m 6 A mRNA Methylation and Gene Transcription by ZFP217 Regulates Pluripotency and Reprogramming. Cell Stem Cell *17*, 689–704. https://doi.org/10.1016/j.stem.2015.09.005.
18. Georgilis, A., Klotz, S., Hanley, C.J., Herranz, N., Weirich, B., Morancho, B., Leote, A.C., D'Artista, L., Gallage, S., Seehawer, M., et al. (2018). PTBP1-Mediated Alternative Splicing Regulates the Inflammatory Secretome and the Pro-tumorigenic Effects of Senescent Cells. Cancer Cell *34*, 85-102.e9. https://doi.org/10.1016/j.ccell.2018.06.007.
19. Neumann, A., Schindler, M., Olofsson, D., Wilhelmi, I., Schürmann, A., and Heyd, F. (2019). Genome-wide identification of alternative splicing events that regulate protein transport across the secretory pathway. J Cell Sci *132*. https://doi.org/10.1242/jcs.230201.
20. Yankova, E., Blackaby, W., Albertella, M., Rak, J., De Braekeleer, E., Tsagkogeorga, G., Pilka, E.S., Aspris, D., Leggate, D., Hendrick, A.G., et al. (2021). Small-molecule inhibition of METTL3 as a strategy against myeloid leukaemia. Nature *593*, 597–601. https://doi.org/10.1038/s41586-021-03536-w.
21. Liu, J., Yue, P., Artym, V. V., Mueller, S.C., and Guo, W. (2009). The Role of the Exocyst in Matrix Metalloproteinase Secretion and Actin Dynamics during Tumor Cell Invadopodia Formation. Mol Biol Cell *20*, 3763–3771. https://doi.org/10.1091/mbc.e08-09-0967.
22. Zeng, Z., Pan, Q., Sun, Y., Huang, H., Chen, X., Chen, T., He, B., Ye, H., Zhu, S., Pu, K., et al. (2023). METTL3 protects METTL14 from STUB1-mediated degradation to maintain m6A homeostasis. EMBO Rep *24*. https://doi.org/10.15252/embr.202255762.
23. Raj, N., Wang, M., Seoane, J.A., Zhao, R.L., Kaiser, A.M., Moonie, N.A., Demeter, J., Boutelle, A.M., Kerr, C.H., Mulligan, A.S., et al. (2022). The Mettl3 epitranscriptomic writer amplifies p53 stress responses. Mol Cell *82*, 2370-2384.e10. https://doi.org/10.1016/j.molcel.2022.04.010.
24. Sorci, M., Ianniello, Z., Cruciani, S., Larivera, S., Ginistrelli, L.C., Capuano, E., Marchioni, M., Fazi, F., and Fatica, A. (2018). METTL3 regulates WTAP protein homeostasis. Cell Death Dis *9*, 796. https://doi.org/10.1038/s41419-018-0843-z.
25. Liu, J., Zuo, X., Yue, P., and Guo, W. (2007). Phosphatidylinositol 4,5-bisphosphate mediates the targeting of the exocyst to the plasma membrane for exocytosis in mammalian cells. Mol Biol Cell. https://doi.org/10.1091/mbc.E07-05-0461.
26. Gallione, C.J., and Rose, J.K. (1985). A single amino acid substitution in a hydrophobic domain causes temperature-sensitive cell-surface transport of a mutant viral glycoprotein. J Virol *54*, 374–382. https://doi.org/10.1128/jvi.54.2.374-382.1985.
27. Paltridge, J.L., Belle, L., and Khew-Goodall, Y. (2013). The secretome in cancer progression. Biochimica et Biophysica Acta (BBA) - Proteins and Proteomics *1834*, 2233–2241. https://doi.org/10.1016/j.bbapap.2013.03.014.

28. Hellinger, J.W., Schömel, F., Buse, J. V., Lenz, C., Bauerschmitz, G., Emons, G., and Gründker, C. (2020). Identification of drivers of breast cancer invasion by secretome analysis: insight into CTGF signaling. Sci Rep *10*, 17889. https://doi.org/10.1038/s41598-020-74838-8.
29. da Cunha, B.R., Domingos, C., Stefanini, A.C.B., Henrique, T., Polachini, G.M., Castelo-Branco, P., and Tajara, E.H. (2019). Cellular Interactions in the Tumor Microenvironment: The Role of Secretome. J Cancer *10*, 4574–4587. https://doi.org/10.7150/jca.21780.
30. Blanco, M.A., LeRoy, G., Khan, Z., Alečković, M., Zee, B.M., Garcia, B.A., and Kang, Y. (2012). Global secretome analysis identifies novel mediators of bone metastasis. Cell Res *22*, 1339–1355. https://doi.org/10.1038/cr.2012.89.
31. Blache, U., Horton, E.R., Xia, T., Schoof, E.M., Blicher, L.H., Schönenberger, A., Snedeker, J.G., Martin, I., Erler, J.T., and Ehrbar, M. (2019). Mesenchymal stromal cell activation by breast cancer secretomes in bioengineered 3D microenvironments. Life Sci Alliance *2*, e201900304. https://doi.org/10.26508/lsa.201900304.
32. Min, J.-W., Kim, W.J., Han, J.A., Jung, Y.-J., Kim, K.-T., Park, W.-Y., Lee, H.-O., Choi, S.S., Bedard, P., Hansen, A., et al. (2015). Identification of Distinct Tumor Subpopulations in Lung Adenocarcinoma via Single-Cell RNA-seq. PLoS One *10*, e0135817. https://doi.org/10.1371/journal.pone.0135817.
33. López de Andrés, J., Griñán-Lisón, C., Jiménez, G., and Marchal, J.A. (2020). Cancer stem cell secretome in the tumor microenvironment: a key point for an effective personalized cancer treatment. J Hematol Oncol *13*, 136. https://doi.org/10.1186/s13045-020-00966-3.
34. Hellinger, J.W., Schömel, F., Buse, J. V., Lenz, C., Bauerschmitz, G., Emons, G., and Gründker, C. (2020). Identification of drivers of breast cancer invasion by secretome analysis: insight into CTGF signaling. Sci Rep *10*, 17889. https://doi.org/10.1038/s41598-020-74838-8.
35. Ziegler, Y.S., Moresco, J.J., Yates, J.R., and Nardulli, A.M. (2016). Integration of Breast Cancer Secretomes with Clinical Data Elucidates Potential Serum Markers for Disease Detection, Diagnosis, and Prognosis. PLoS One *11*, e0158296. https://doi.org/10.1371/journal.pone.0158296.
36. Alpha, K.M., Xu, W., and Turner, C.E. (2020). Paxillin family of focal adhesion adaptor proteins and regulation of cancer cell invasion. In, pp. 1–52. https://doi.org/10.1016/bs.ircmb.2020.05.003.
37. Kumari, K., Groza, P., and Aguilo, F. (2021). Regulatory roles of RNA modifications in breast cancer. NAR Cancer *3*. https://doi.org/10.1093/narcan/zcab036.
38. Barbieri, I., Tzelepis, K., Pandolfini, L., Shi, J., Millán-Zambrano, G., Robson, S.C., Aspris, D., Migliori, V., Bannister, A.J., Han, N., et al. (2017). Promoter-bound METTL3 maintains myeloid leukaemia by m6A-dependent translation control. Nature *552*, 126–131. https://doi.org/10.1038/nature24678.
39. Wang, X., and Li, S. (2014). Protein mislocalization: Mechanisms, functions and clinical applications in cancer. Biochimica et Biophysica Acta (BBA) - Reviews on Cancer *1846*, 13–25. https://doi.org/10.1016/j.bbcan.2014.03.006.
40. Liu, C., Yu, M., Wang, M., Yang, S., Fu, Y., Zhang, L., Zhu, C., and Zhang, H. (2024). PCAF-mediated acetylation of METTL3 impairs mRNA translation efficiency in response to oxidative stress. Sci China Life Sci *67*, 2157–2168. https://doi.org/10.1007/s11427-023-2535-x.

41. Li, Y., He, X., Lu, X., Gong, Z., Li, Q., Zhang, L., Yang, R., Wu, C., Huang, J., Ding, J., et al. (2022). METTL3 acetylation impedes cancer metastasis via fine-tuning its nuclear and cytosolic functions. Nat Commun *13*, 6350. https://doi.org/10.1038/s41467-022-34209-5.
42. Huang, X., Zhang, J., Cun, Y., Ye, M., Ren, Z., Guo, W., Ma, X., Liu, J., Luo, W., Sun, X., et al. (2025). Spatial control of m6A deposition on enhancer and promoter RNAs through co-acetylation of METTL3 and H3K27 on chromatin. Mol Cell *85*, 1349-1365.e10. https://doi.org/10.1016/j.molcel.2025.02.016.
43. Yau, C., Esserman, L., Moore, D.H., Waldman, F., Sninsky, J., and Benz, C.C. (2010). A multigene predictor of metastatic outcome in early stage hormone receptor-negative and triple-negative breast cancer. Breast Cancer Research *12*, R85. https://doi.org/10.1186/bcr2753.
44. Liu, P., Li, F., Lin, J., Fukumoto, T., Nacarelli, T., Hao, X., Kossenkov, A. V., Simon, M.C., and Zhang, R. (2021). m6A-independent genome-wide METTL3 and METTL14 redistribution drives the senescence-associated secretory phenotype. Nat Cell Biol *23*, 355–365. https://doi.org/10.1038/s41556-021-00656-3.
45. Moser, J.C., Papadopoulos, K.P., Rodon Ahnert, J., Ofir-Rosenfeld, Y., and Holz, J.-B. (2024). Phase 1 dose escalation and cohort expansion study evaluating safety, PK, PD and clinical activity of STC-15, a METTL-3 inhibitor, in patients with advanced malignancies. Journal of Clinical Oncology *42*, 2586–2586. https://doi.org/10.1200/JCO.2024.42.16_suppl.2586.
46. Békés, M., Langley, D.R., and Crews, C.M. (2022). PROTAC targeted protein degraders: the past is prologue. Nat Rev Drug Discov *21*, 181–200. https://doi.org/10.1038/s41573-021-00371-6.
47. Baj-Krzyworzeka, M., Szatanek, R., Węglarczyk, K., Baran, J., Urbanowicz, B., Brański, P., Ratajczak, M.Z., and Zembala, M. (2006). Tumour-derived microvesicles carry several surface determinants and mRNA of tumour cells and transfer some of these determinants to monocytes. Cancer Immunology, Immunotherapy *55*, 808–818. https://doi.org/10.1007/s00262-005-0075-9.
48. Valadi, H., Ekström, K., Bossios, A., Sjöstrand, M., Lee, J.J., and Lötvall, J.O. (2007). Exosome-mediated transfer of mRNAs and microRNAs is a novel mechanism of genetic exchange between cells. Nat Cell Biol *9*, 654–659. https://doi.org/10.1038/ncb1596.
49. O'Brien, K., Breyne, K., Ughetto, S., Laurent, L.C., and Breakefield, X.O. (2020). RNA delivery by extracellular vesicles in mammalian cells and its applications. Nat Rev Mol Cell Biol *21*, 585–606. https://doi.org/10.1038/s41580-020-0251-y.
50. Tosar, J.P., Witwer, K., and Cayota, A. (2021). Revisiting Extracellular RNA Release, Processing, and Function. Trends Biochem Sci *46*, 438–445. https://doi.org/10.1016/j.tibs.2020.12.008.
51. Batey, R.T., Rambo, R.P., Lucast, L., Rha, B., and Doudna, J.A. (2000). Crystal Structure of the Ribonucleoprotein Core of the Signal Recognition Particle. Science (1979) *287*, 1232–1239. https://doi.org/10.1126/science.287.5456.1232.
52. MacIntosh, G.C., Bariola, P.A., Newbigin, E., and Green, P.J. (2001). Characterization of Rny1, the *Saccharomyces cerevisiae* member of the T_2 RNase family of RNases: Unexpected functions for ancient enzymes? Proceedings of the National Academy of Sciences *98*, 1018–1023. https://doi.org/10.1073/pnas.98.3.1018.
53. Lin, A., Hu, Q., Li, C., Xing, Z., Ma, G., Wang, C., Li, J., Ye, Y., Yao, J., Liang, K., et al. (2017). The LINK-A lncRNA interacts with PtdIns(3,4,5)P3 to hyperactivate AKT and

confer resistance to AKT inhibitors. Nat Cell Biol *19*, 238–251. https://doi.org/10.1038/ncb3473.

54. Tcherkezian, J., Brittis, P.A., Thomas, F., Roux, P.P., and Flanagan, J.G. (2010). Transmembrane Receptor DCC Associates with Protein Synthesis Machinery and Regulates Translation. Cell *141*, 632–644. https://doi.org/10.1016/j.cell.2010.04.008.
55. Francesca, G., Cinzia, P., Antonella, B., Stefano, F.-V., Teresa, C.M., Tiziano, I., Annalisa, O., Martine, A.-T., Nicoletta, C., Nadia, C., et al. (2016). SMN affects membrane remodelling and anchoring of the protein synthesis machinery. J Cell Sci. https://doi.org/10.1242/jcs.176750.
56. Mardakheh, F.K., Paul, A., Kümper, S., Sadok, A., Paterson, H., Mccarthy, A., Yuan, Y., and Marshall, C.J. (2015). Global Analysis of mRNA, Translation, and Protein Localization: Local Translation Is a Key Regulator of Cell Protrusions. Dev Cell *35*, 344–357. https://doi.org/10.1016/j.devcel.2015.10.005.
57. Ren, J., and Guo, W. (2012). ERK1/2 Regulate Exocytosis through Direct Phosphorylation of the Exocyst Component Exo70. Dev Cell *22*, 967–978. https://doi.org/10.1016/j.devcel.2012.03.005.
58. Berginski, M.E., and Gomez, S.M. (2013). The Focal Adhesion Analysis Server: a web tool for analyzing focal adhesion dynamics. F1000Res *2*, 68. https://doi.org/10.12688/f1000research.2-68.v1.
59. Kechagia, Z., Sáez, P., Gómez-González, M., Canales, B., Viswanadha, S., Zamarbide, M., Andreu, I., Koorman, T., Beedle, A.E.M., Elosegui-Artola, A., et al. (2023). The laminin–keratin link shields the nucleus from mechanical deformation and signalling. Nat Mater *22*, 1409–1420. https://doi.org/10.1038/s41563-023-01657-3.
60. Hughes, C.S., Foehr, S., Garfield, D.A., Furlong, E.E., Steinmetz, L.M., and Krijgsveld, J. (2014). Ultrasensitive proteome analysis using paramagnetic bead technology. Mol Syst Biol *10*. https://doi.org/10.15252/msb.20145625.
61. Mateus, A., Hevler, J., Bobonis, J., Kurzawa, N., Shah, M., Mitosch, K., Goemans, C. V., Helm, D., Stein, F., Typas, A., et al. (2020). The functional proteome landscape of Escherichia coli. Nature *588*, 473–478. https://doi.org/10.1038/s41586-020-3002-5.
62. Kong, A.T., Leprevost, F. V, Avtonomov, D.M., Mellacheruvu, D., and Nesvizhskii, A.I. (2017). MSFragger: ultrafast and comprehensive peptide identification in mass spectrometry–based proteomics. Nat Methods *14*, 513–520. https://doi.org/10.1038/nmeth.4256.
63. Huber, W., von Heydebreck, A., Sültmann, H., Poustka, A., and Vingron, M. (2002). Variance stabilization applied to microarray data calibration and to the quantification of differential expression. Bioinformatics *18*, S96–S104. https://doi.org/10.1093/bioinformatics/18.suppl_1.S96.
64. Ritchie, M.E., Phipson, B., Wu, D., Hu, Y., Law, C.W., Shi, W., and Smyth, G.K. (2015). limma powers differential expression analyses for RNA-sequencing and microarray studies. Nucleic Acids Res *43*, e47–e47. https://doi.org/10.1093/nar/gkv007.

FIGURES AND LEGENDS

Figure 1

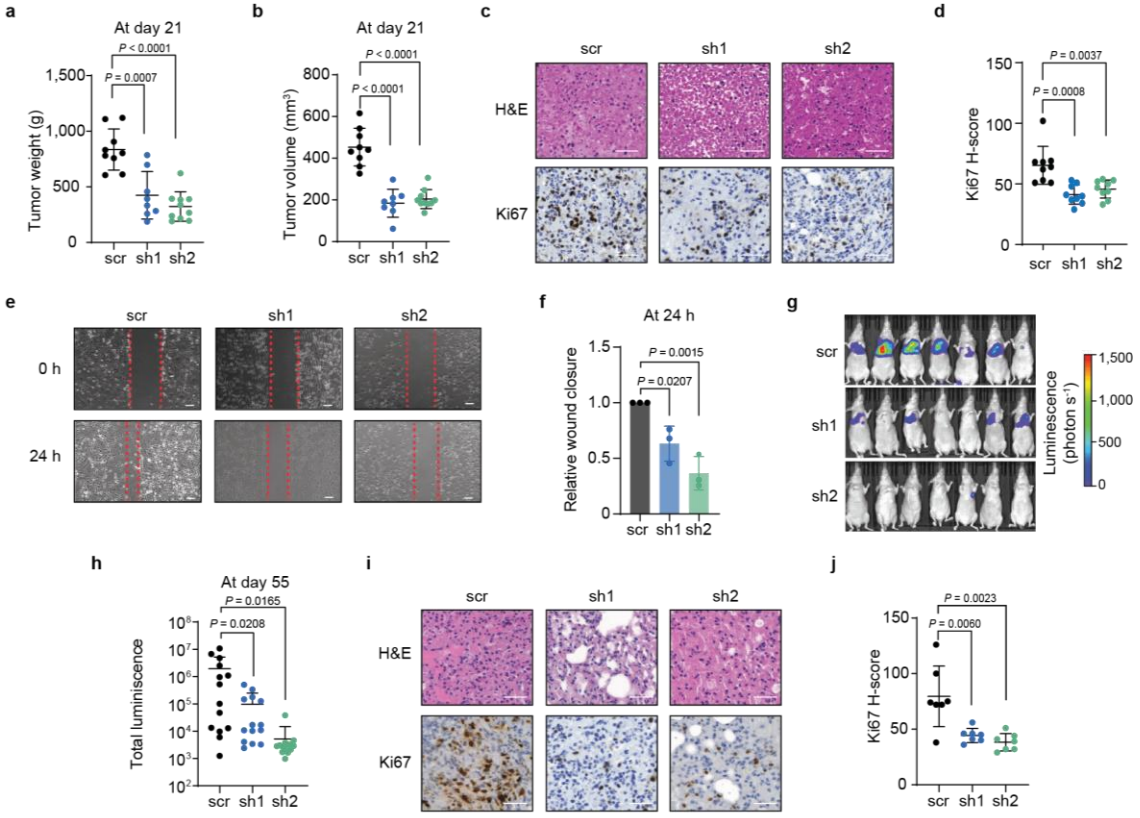

Figure legend in the next page.

Figure 1: METTL3 promotes cancer growth and metastasis in vivo.

a,**b**, Tumor weight (**a**) and tumor volume (**b**) were measured in mice injected with control (scramble (scr)) or METTL3-knockdown (sh1 and sh2) MDA-MB-231 cells. n = 9. **c,** Haematoxylin and eosin (H&E, top) and Ki67 (bottom) staining of breast sections from mice injected with scramble (scr) or METTL3-knockdown (sh1 and sh2) MDA-MB-231 cells in the mammary fat pads. Scale bars, 50 μm **d,** Quantification of Ki67 staining in breast sections from mice injected with control (scr) or METTL3-knockdown (sh1 and sh2) MDA-MB-231 cells from (**c**.) The intensity of the staining is associated with an H-score value (Methods). **e,** Wound healing assay assessed in scramble (scr) or METTL3-depleted (sh1 and sh2) MDA-MB-231 cells. Scale bars, 50 μm. **f,** Bar graph illustrating relative wound closure at 24 h during the wound healing assay. **g,** Bioluminescence imaging of mice injected with control (scr) or METTL3-knockdown (sh1 and sh2) MDA-MB-231 cells, showing reduced metastasis formation upon depletion of METTL3 at day 55. Scale represents the luminescence detected per pixel. **h,** Quantification of total luminescence (sum for all the pixels) established on the ventral and dorsal sides of the mice (n = 9). **i,** H&E (top) and Ki67 (bottom) staining of lung sections from mice injected with scramble (scr) or METTL3-knockdown (sh1 and sh2) MDA-MB-231 cells via the tail vein. Scale bars, 50 μm **j,** Quantification of Ki67 staining in lung sections from mice injected with control (scr) or METTL3-knockdown (sh1 and sh2) MDA-MB-231 cells from (**i**). The intensity of the staining is associated with a H-score value. Data are mean ± s.d. Two-tailed Student's t-test (**a**,**b**,**d**,**h**,**j**) and one-way ANOVA with Dunnett's correction for multiple comparison (**f**).

Figure 2

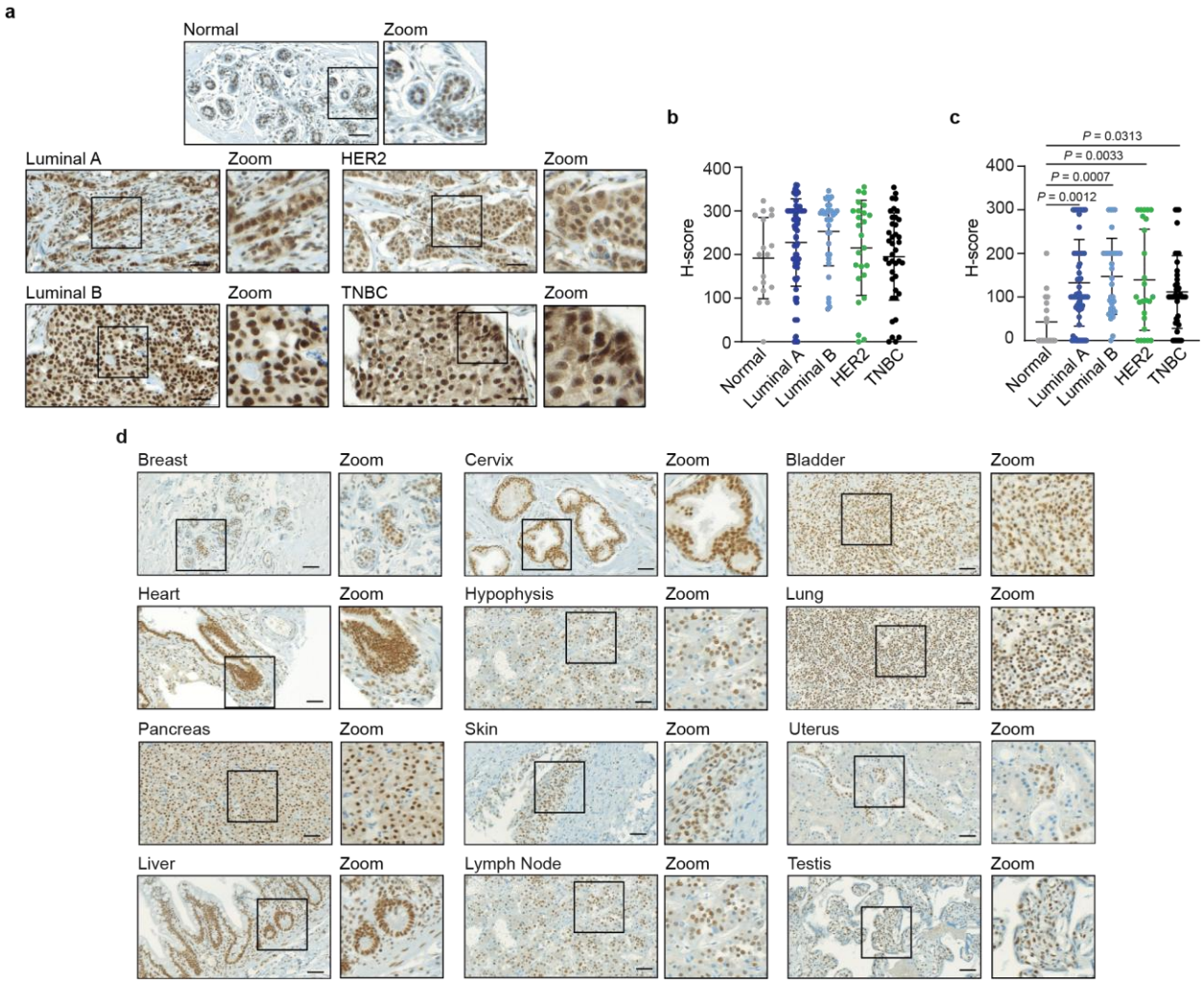

Figure 2: METTL3 is mislocalized in breast cancer cells.

a, IHC staining of METTL3 in normal epithelial tissue and breast cancer tissues from patients. Scale bars, 50 µm. **b,c,** Quantification of IHC detection of METTL3 in the nucleus (**b**) and the cytoplasm (**c**) from (**a**). **d,** IHC staining of METTL3 in various normal healthy tissues, including breast, cervix, bladder, heart, hypophysis, lung, pancreas, skin, uterus, liver, lymph node, and testis. Scale bars, 50 µm. Data are mean ± s.d. One-way ANOVA with Dunnett's correction for multiple comparison (**b**,**c**).

Figure 3

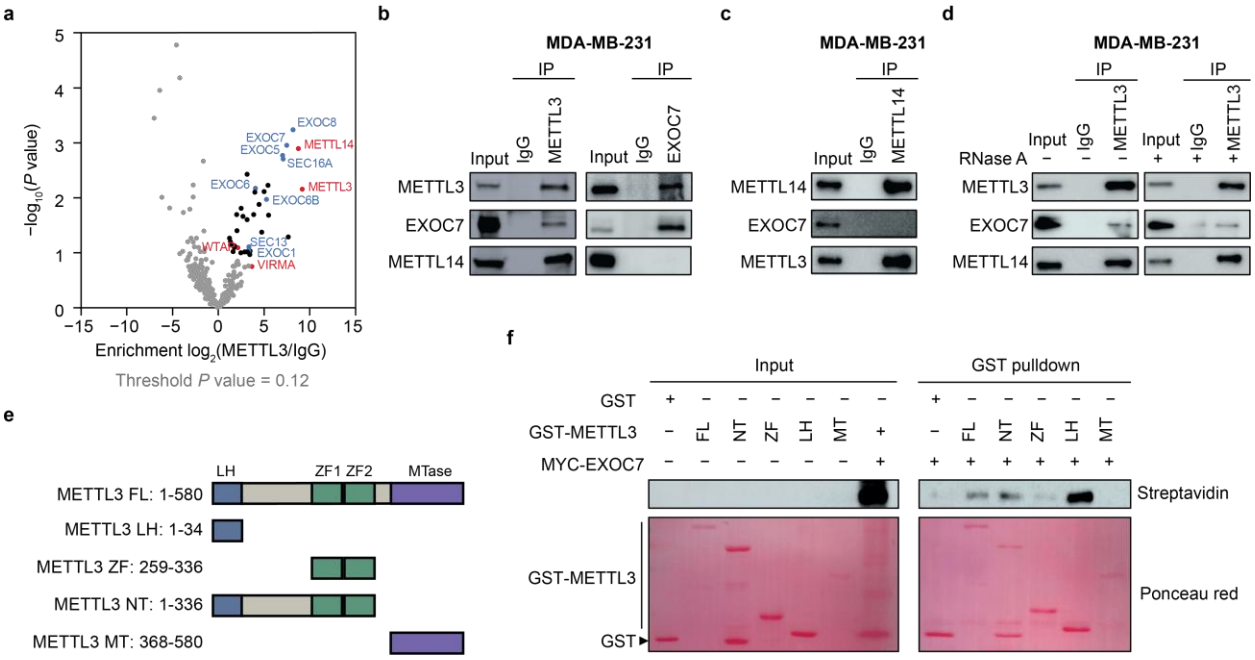

Figure legend in the next page.

Figure 3: METTL3 interacts with subunits of the exocyst.

a, Volcano plot of METTL3-interacting proteins in the cytoplasm of MCF7 cells. $P < 0.12$ and $\log_2$ (METTL3/IgG) > 1 are used as thresholds. IgG is used as the negative control. The percentage of input used is 10%. **b,c,** Immunoprecipitation (IP) of cytoplasmic extracts from MDA-MB-231 with antibodies against METTL3 and EXOC7 (**b**) and METTL14 (**c**) followed by immunoblotting with METTL3, EXOC7 and METTL14. IgG is used as the negative control. The percentage of input used is 10%. **d,** Immunoprecipitation of cytoplasmic extracts from MDA-MB-231 pretreated with RNase A with antibodies against METTL3 and EXOC7 followed by immunoblotting with METTL3, EXOC7 an METTL14. IgG is used as the negative control. Percentage of input is 10%. **e,** Schematic representation of GST–METTL3 purified proteins for in vitro pull-down analysis: GST–METTL3 full-length (FL), GST–N-terminal domain (NT), GST–zinc-finger domains (ZF), GST–leader-helix domain (LH) and GST–methylase-domain (MT). **f,** GST pull-down assay with in vitro transcribed and translated MYC–EXOC7. Immunoblotting of MYC–EXOC7 was detected using Streptavidin–HRP. GST-tagged proteins were detected with Ponceau red staining. GST alone was used as the negative control. The percentage of input used for the MYC–EXOC proteins is 1% and 10% for the GST-tagged proteins. Images are representative of three independently performed experiments with similar results.

Figure 4

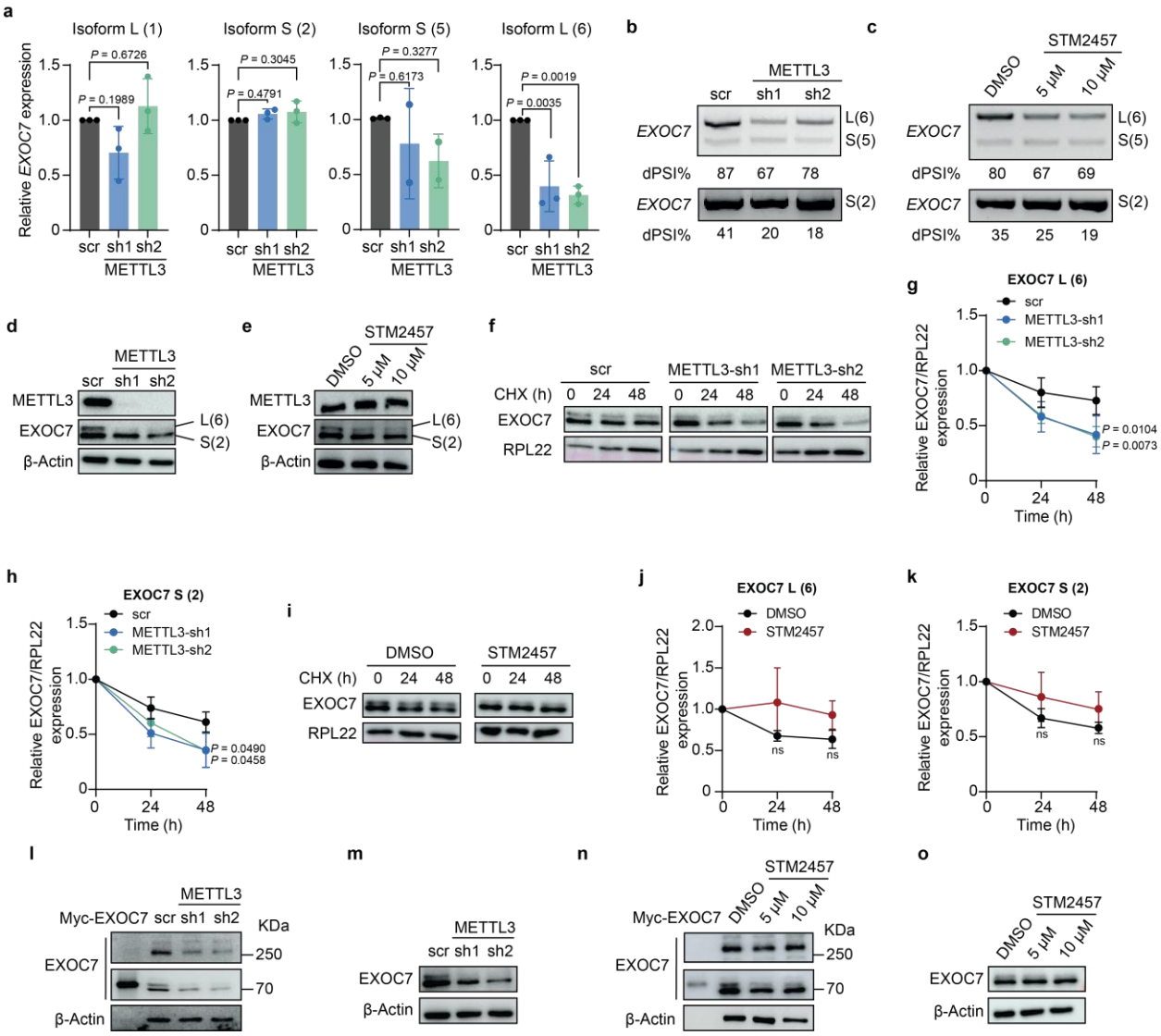

Figure legend in the next page.

Figure 4: METTL3 regulates EXOC7 alternative splicing and the exocyst function.

a, Quantitative PCR with reverse transcription (RT–qPCR) analysis of *EXOC7* isoforms in scramble (scr) and METTL3-knockdown (sh1, sh2) cells. **b,** RT–PCR showing exon-skipping event in *EXOC7* transcript in scramble (scr) and METTL3-knockdown (sh1, sh2) cells. Delta Percent Spliced-In (dPSI%) represents the change in exon inclusion levels between conditions. **c,** RT–PCR showing exon-skipping event in *EXOC7* transcript in DMSO (control)- and STM2457-treated cells at indicated concentrations. dPSI% is indicated. **d,** Western blot of METTL3 and EXOC7 from whole-cell extracts from scramble (scr) and METTL3-knockdown (sh1, sh2) MDA-MB-231 cells showing EXOC7 protein isoforms. **e,** Western blot of METTL3 and EXOC7 from whole cell extracts from DMSO (control) and STM2457 treated cells at indicated concentrations. **f,** Western blots of EXOC7 from scramble (scr) and METTL3-knockdown (sh1, sh2) HEK293T cells during a 48 h CHX time course treatment. RPL22 is used as the loading control. **g,** Protein degradation curve of EXOC7 long isoform (6) during 48 h of CHX treatment generated from (**f**). *P* values at 24 h: METTL3-sh1 = 0.0292; METTL3-sh2 = 0.0363. Protein expression is normalized to RPL22 and relative to time 0 h. **h,** Protein degradation curve of EXOC7 short isoform (2) during 48 h of CHX treatment generated from (**f**). *P* values at 24 h: METTL3-sh1 = 0.0495; METTL3-sh2 = 0.2470. Protein expression is normalized to RPL22 and relative to time 0 h. **i,** Western blots of EXOC7 from DMSO- (control) and STM2457-treated HEK293T cells during a 48 h CHX time course treatment. RPL22 is used as the loading control. **j,** Protein degradation curve of EXOC7 long isoform (6) during 48 h of CHX treatment generated from (**i**). Protein expression is normalized to RPL22 and relative to time 0 h. **k,** Protein degradation curve of EXOC7 short isoform (2) during 48 h of CHX treatment generated from (**i**). Protein expression is normalized to RPL22 and relative to time 0 h. **l,** Non-reducing PAGE of EXOC7 from in vitro transcribed and translated Myc-EXOC7, scramble (scr) and METTL3-knockdown (sh1, sh2) MDA-MB-231 cells. β-Actin is used as the loading control. **m,** Western blot of EXOC7 from scramble (scr) and METTL3-knockdown (sh1, sh2) MDA-MB-231. β-Actin is used as the loading control. **n,** Non-reducing PAGE of EXOC7 from in vitro transcribed and translated Myc-EXOC7, DMSO (control)- and STM2457-treated MDA-MB-21 cells at indicated concentrations. β-Actin is used as the loading control. **o,** Western blot of EXOC7 from whole cell extracts from DMSO (control) and STM2457 treated cells at indicated concentrations. β-Actin is used as the loading control.

Figure 5

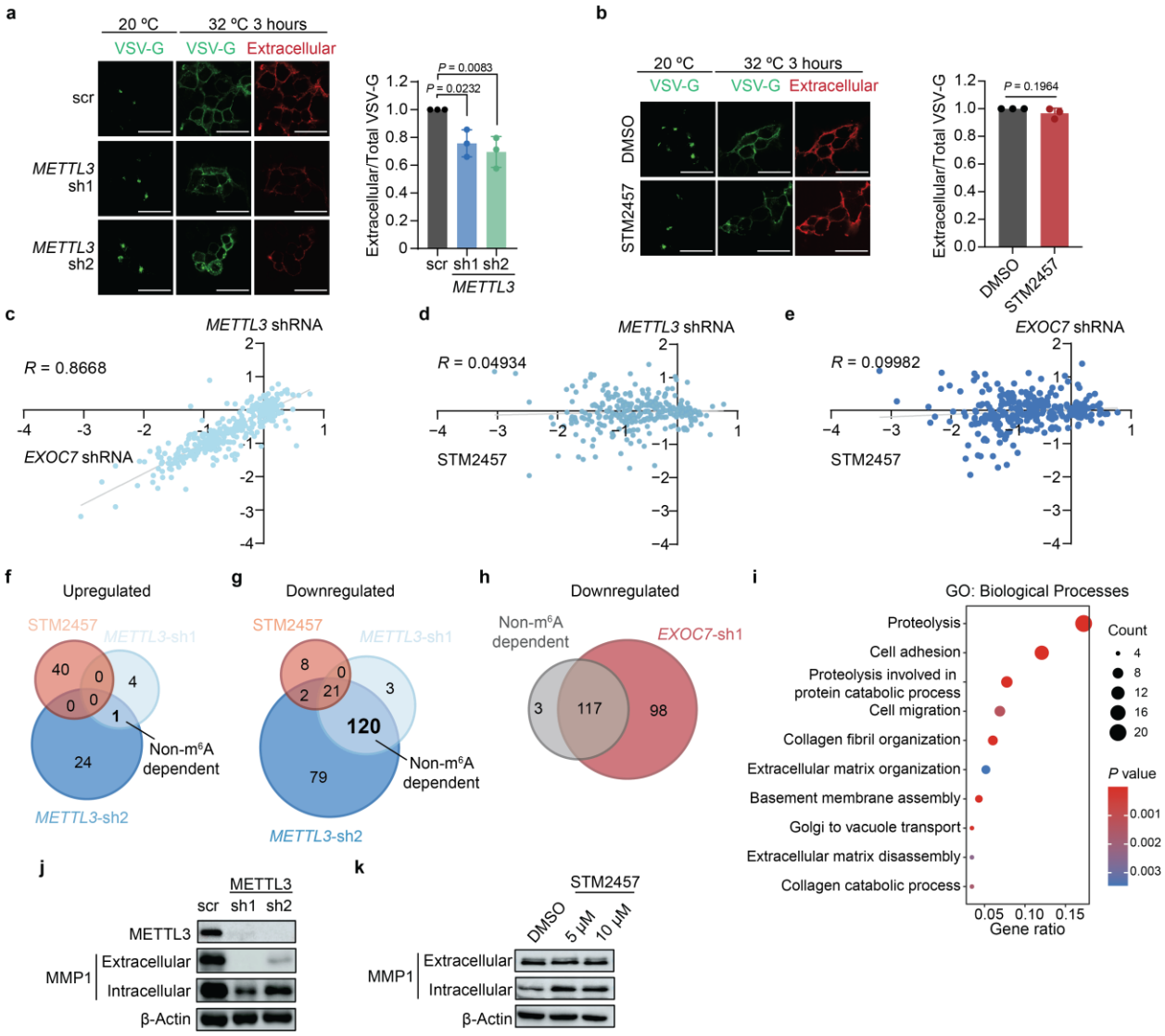

Figure legend in the next page.

Figure 5: METTL3 is involved in vesicle trafficking regulation and modulates the secretome in MDA-MB-231 breast cancer cell line.

a, Left, immunofluorescence images of control (scr) and METTL3-knockdown (sh1 and sh2) HEK293T cells expressing GFP-VSV-Gts045 and collected after 3 h at 32 ºC, then stained with the 8G5 antibody to visualize VSV-G incorporation into the plasma membrane. Scale bars, 30 µm. Right, quantification shows the ratio of extracellular (8G5 staining) to total cellular VSV-G fluorescence. **b,** Left, immunofluorescence images of HEK293T cells expressing GFP-VSV-Gts045 treated with DMSO (control) or STM2457 inhibitor after 3 h at 32 ºC. Scale bars, 30 µm. Right, quantification shows the ratio of extracellular (8G5 staining) to total cellular VSV-G fluorescence. **c–e,** Correlation of secretome profiles between METTL3 and EXOC7 knockdowns (**c**), METTL3 knockdowns and STM2457-treated cells (**d**), and EXOC7 knockdowns and STM2457-treated cells (**e**). Proteins in common between different conditions were used to generate the plots. **f,** Overlap between upsecreted proteins from METTL3-knockdown (sh1 and sh2) and STM2457 treated MDA-MB-231 cells ($\log_2$ fold change (FC) < 0 and false discovery rate (FDR) < 0.05). **g,** Overlap between proteins that exhibit downregulated secretion (downsecreted proteins) in METTL3-knockdown (sh1 and sh2) compared with STM2457 treated MDA-MB-231 cells ($\log_2$FC < 0 and FDR < 0.05). **h,** Overlap between downsecreted non-m^6A-dependent proteins identified in **g** and upon EXOC7 knockdown (sh1 and sh2) ($\log_2$FC < 0 and FDR < 0.05). **i,** Gene ontology (GO) analysis of biological processes related to the common downsecreted proteins identified in **h**. **j**, Western blot of METTL3, intracellular and extracellular MMP1 from scramble (scr) and METTL3-knockdown (sh1, sh2) MDA-MB-231 cells showing lower secretion of MMP1 compared to intracellular levels. **k**, Western blot of intracellular and extracellular MMP1 from DMSO- and STM2457-treated cells showing no defect in MMP1 secretion compared to intracellular levels upon METTL3 inhibition. Data are mean ± s.d. One-way ANOVA with Dunnett's correction for multiple comparison (**a**) and two-tailed Student's t-test (**b**).

Figure 6

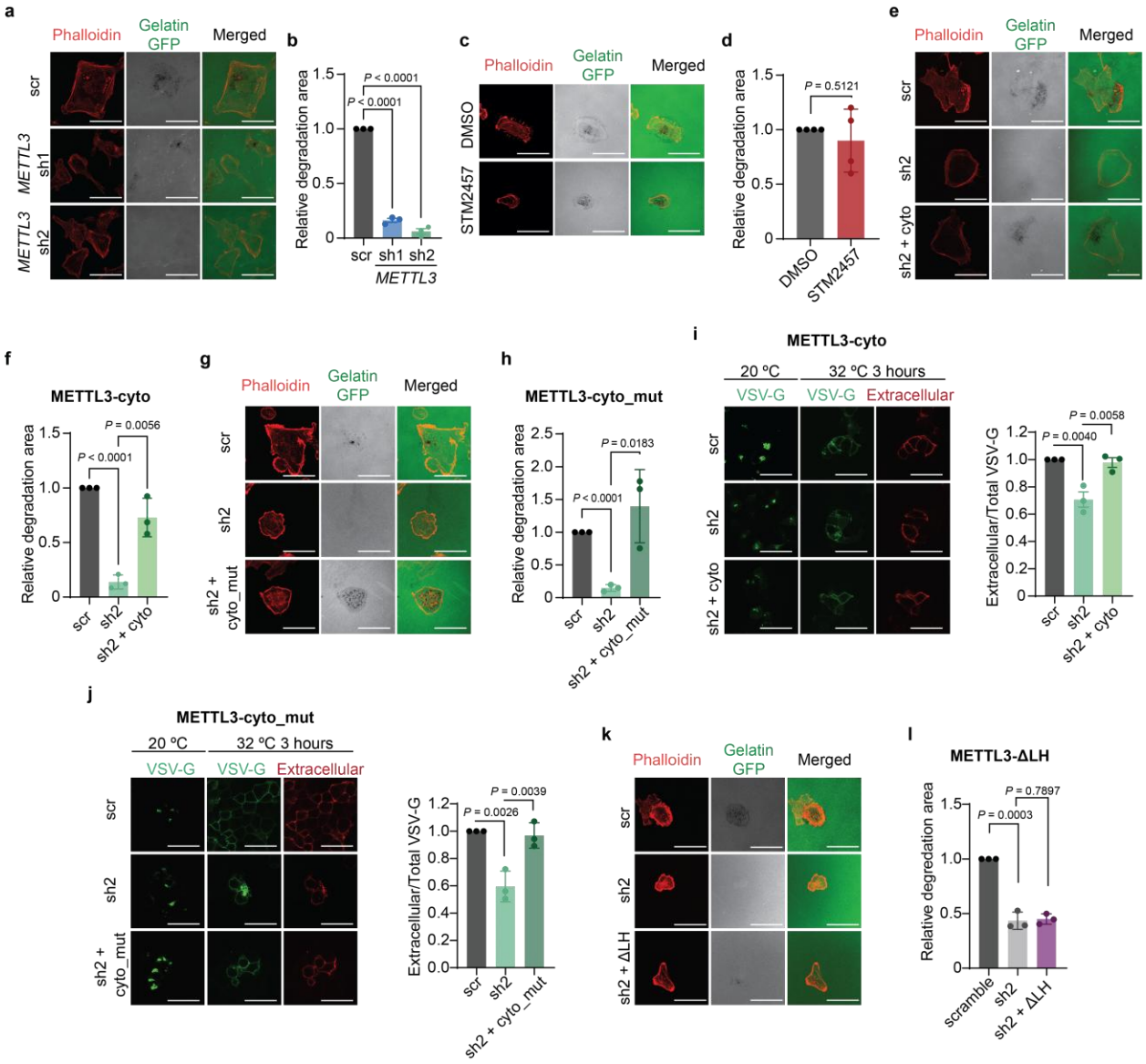

Figure legend in the next page.

Figure 6: METTL3 promotes tumor cell invasion by facilitating ECM degradation through invadopodia formation.

a, Gelatin-degradation assay of MDA-MB-231 showing reduced invadopodia formation upon depletion of METTL3 (sh1 and sh2) compared with control (scr). Cells were cultured on Alexa-488 gelatin coated coverslips. Phalloidin is used as an F-actin marker. Scale bars, 40 µm. **b**, Quantification of areas of degradation corresponding to invadopodia formation in (**a**). **c,** Gelatin-degradation assay of MDA-MB-231 showing no impairment of invadopodium formation upon STM2457 (5 µM) treatment. Cells were cultured on Alexa-488 gelatin coated coverslips. Phalloidin is used as an F-actin marker. **d,** Quantification of areas of degradation corresponding to invadopodia formation in (**c**). **e,** Gelatin-degradation assay of MDA-MB-231 showing the rescue of the invadopodia formation defect (sh2 + cyto) compared to the knockdown of *METTL3* (sh2). Phalloidin is used as an F-actin marker. Scale bars, 40 µm. **f,** Quantification of areas of degradation corresponding to invadopodia formation in (**e**). **g,** Gelatin-degradation assay of MDA-MB-231 showing the rescue of invadopodia formation defect upon expression of catalytically dead cytoplasmic METTL3 (sh2 + cyto_mut) compared to the knockdown of *METTL3* (sh2). Phalloidin is used as an F-actin marker. Scale bars, 40 µm. **h,** Quantification of areas of degradation corresponding to invadopodia formation in (**g**). **i,** Left, immunofluorescence images showing the rescue of the vesicle trafficking (sh2 + cyto) compared to the knockdown of *METTL3* (sh2) of HEK293T cells expressing GFP-VSV-Gts045 and collected after 3 h at 32 ºC, then stained with the 8G5 antibody to visualize VSV-G incorporation into the plasma membrane. Scale bars, 30 µm. Right, quantification shows the ratio of extracellular (8G5 staining) to total cellular VSV-G fluorescence. **j,** Left, immunofluorescence images showing the rescue of the vesicle trafficking (sh2 + cyto_mut) compared to the knockdown of *METTL3* (sh2) of HEK293T cells expressing GFP-VSV-Gts045 and collected after 3 h at 32 ºC, then stained with the 8G5 antibody to visualize VSV-G incorporation into the plasma membrane. Scale bars, 30 µm. Right, quantification shows the ratio of extracellular (8G5 staining) to total cellular VSV-G fluorescence. **k,** Gelatin-degradation assay of MDA-MB-231 showing the rescue of invadopodia formation defect upon expression of ΔLH–METTL3 (sh2 + ΔLH) cells compared to the knockdown of *METTL3* (sh2). Phalloidin is used as an F-actin marker. Scale bars, 40 µm. **l,** Quantification of areas of degradation corresponding to invadopodia formation from (**k**). Data are mean ± s.d. Two-tailed Student's *t*-test (**b,d,f,h-k**).

Figure 7

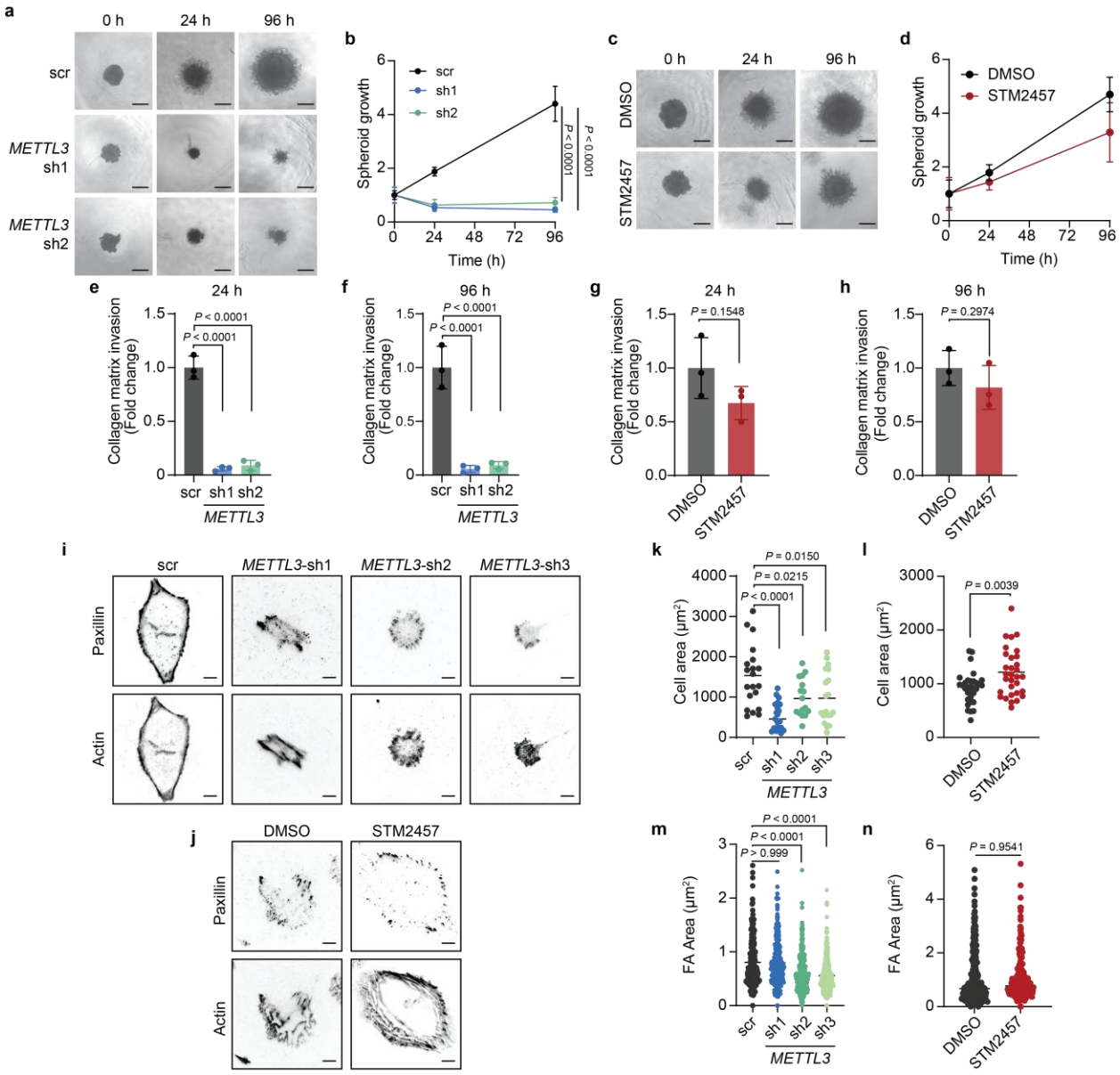

Figure legend in the next page.

Figure 7. Functional impact of depletion and inhibition of METTL3 in invasion and cell adhesion.

a, Illustrative example of anchorage-independent spheroid growth of scramble (scr) and METTL3-knockdown (sh1, sh2) MDA-MB-231 cells. Scarle bars, 200 µm. **b**, Spheroid growth measured after embedding scramble (scr) or METTL3-knockdown (sh1, sh2) MDA-MB-21 cells in Matrigel® Matrix at 24 and 96 h, relative to time 0. **c**, Illustrative example of anchorage-independent spheroid growth MDA-MB-231 cells treated with DMSO (control) or STM2457 inhibitor (10 µM). Scarle bars, 200 µm. **d**, Spheroid growth measured after embedding DMSO or STM2457 treated cells in Matrigel® Matrix at 24 and 96 h, relative to time 0 h. **e,f**, Quantification of spheroid invasive area at 24 h (**e**) and 96 h (**f**) of scramble (scr) or METTL3-knockdown (sh1, sh2) MDA-MB-231 cells. **g,h**, Quantification of spheroid invasive area at 24 h (**g**) and 96 h (**h**) of DMSO- and STM2457-treated MDA-MB-231 cells. **i,** Representative images of scramble (scr) and METTL3-knockdown (sh1, sh2, sh3). **j,** Representative images of DMSO- and STM2457-treated (10 µM) MDA-MB-231 cells on glass coated with 10 µg/ml of collagen I, fixed, and stained with Phalloidin-594 to label actin, and Alexa-488 to label Paxillin. Scale bar, 10 µm. **k,l,** Box plot quantification of cell area from analysis of immunofluorescence images of scramble (scr) and METTL3-knockdown (sh1, sh2, sh3) MDA-MB-231 cells (**k**) and DMSO- (control) and STM2457- treated MDA-MB-231 cells (**l**). **m,n,** Box plot of focal adhesion area of scramble (scr) and METTL3-knockdown (sh1, sh2, sh3) MDA-MB-231 cells (**m**) and DMSO- (control) and STM2457- treated MDA-MB-231 cells (**n**). Quantifications were from analysis of immunofluorescence images of paxillin. Each point represents an average of 10 FAs per cell. N= 21 (sr), 19 (METTL3-sh1), 19 (METTL3-sh2), 21 (METTL3-sh3), 21 (DMSO) 20 (STM2457), respectively. Data are mean ± s.d. Two-way ANOVA with Dunnett's correction for multiple comparison (**b,d**), one-way ANOVA with Dunnett's correction for multiple comparison (**e,f,k**), two-tailed Student's *t*-test (**g,h, l, n**), Krustal-Wallis test (**m**).